The Multi-Scale Interactions of Atmospheric Phenomenon in Extreme and Mean Precipitation

Andreas Franz Prein[1], Priscilla A. Mooney[2], and James Done[1]

[1]National Center for Atmospheric Research (UCAR)
[2]NORCE Norwegian Research Centre

February 9, 2023

Abstract

Globally, extreme precipitation events cause enormous impacts. Climate change increases the frequency and intensity of extreme precipitation, which in combination with rising population enhances exposure to major floods. An improved understanding of the atmospheric processes that cause extreme precipitation events would help to advance predictions and projections of such events. To date, such analyses have typically been performed rather unsystematically and over limited areas (e.g., the U.S.) which has resulted in contradictory findings. Here we present the Multi Object Analysis of Atmospheric Phenomenon (MOAAP) algorithm that uses a set of nine common atmospheric variables to identify and track tropical and extra-tropical cyclones, anticyclones, atmospheric rivers (ARs), mesoscale convective systems (MCSs), and frontal zones. We apply the algorithm to global historical data between 2000 to 2020. We find that MCSs produce the vast majority of extreme precipitation in the tropics and some mid-latitude land regions, while extreme precipitation in mid- and high-latitude ocean and coastal regions are dominated by cyclones and ARs. Importantly, most extreme precipitation events are associated with interacting features across scales that intensify precipitation. These interactions, however, can be a function of the rarity (e.g., return period) of extreme events. The presented methodology and results could have wide-ranging applications including training of machine learning methods, lagrangian-based evaluation of climate models, and process-based understanding of extreme precipitation in a changing climate.

The Multi-Scale Interactions of Atmospheric Phenomenon in Extreme and Mean Precipitation

Andreas F. Prein[1], Priscilla A. Mooney[2], James M. Done[1]

[1]National Center for Atmospheric Research
[2]NORCE, Bjerknes Centre for Climate Research

Key Points:

- A novel algorithm simultaneously tracks cyclones, anticyclones, MCSs, atmospheric rivers, and fronts.
- Extreme precipitation is typically associated with multiple atmospheric phenomena that interact across scales.
- MCSs are involved in most extreme precipitation events in the tropics and many sub-tropical and mid-latitude regions.

Corresponding author: Andreas F. Prein, prein@ucar.edu

Abstract

Globally, extreme precipitation events cause enormous impacts. Climate change increases the frequency and intensity of extreme precipitation, which in combination with rising population enhances exposure to major floods. An improved understanding of the atmospheric processes that cause extreme precipitation events would help to advance predictions and projections of such events. To date, such analyses have typically been performed rather unsystematically and over limited areas (e.g., the U.S.) which has resulted in contradictory findings. Here we present the Multi Object Analysis of Atmospheric Phenomenon (MOAAP) algorithm that uses a set of nine common atmospheric variables to identify and track tropical and extra-tropical cyclones, anticyclones, atmospheric rivers (ARs), mesoscale convective systems (MCSs), and frontal zones. We apply the algorithm to global historical data between 2000 to 2020. We find that MCSs produce the vast majority of extreme precipitation in the tropics and some mid-latitude land regions, while extreme precipitation in mid- and high-latitude ocean and coastal regions are dominated by cyclones and ARs. Importantly, most extreme precipitation events are associated with interacting features across scales that intensify precipitation. These interactions, however, can be a function of the rarity (e.g., return period) of extreme events. The presented methodology and results could have wide-ranging applications including training of machine learning methods, lagrangian-based evaluation of climate models, and process-based understanding of extreme precipitation in a changing climate.

Plain Language Summary

Increases in intense precipitation and faster onsets of droughts are just two of many precipitation related extreme events that worsen under progressive climate change. Surprisingly little is know about the weather systems that are driving these changes in many regions around the world. In order to better predict and prepare for these events, scientists need an improved understanding of the causes of the involved atmospheric processes and their interactions. A new algorithm called the Multi Object Analysis of Atmospheric Phenomenon (MOAAP) has been developed to identify and track different types of weather systems, such as tropical and extra-tropical cyclones, that can lead to extreme precipitation. The algorithm was applied to global weather data from 2000 to 2020. The results showed that certain types of weather systems, such as mesoscale convective systems, are frequently involved in causing the most extreme precipitation. Additionally, the study found that most extreme precipitation events are caused by a combination of different weather systems working together, and that these interactions can vary for very rare and more common extreme events. This research could be useful for improving climate models and understanding how extreme precipitation is likely to change in the future.

1 Introduction

Many studies have examined the atmospheric drivers of intense precipitation. Kunkel et al. (2012) analyzed the drivers of 1-in-5-year occurrence of daily precipitation events in the U.S. during the period 1908–2009 and found that more than 70 % of extreme precipitation in the central U.S. is related to frontal systems and less than 10 % to mesoscale convective systems (MCSs). In similar work, Schumacher and Johnson (2006) found a much greater contribution from MCSs of 75 % of warm-season intense precipitation events in the eastern U.S. This highlights: (i) the difficulty in differentiating the dominant phenomena that cause intense precipitation and (ii) that intense events may be influenced by multiple phenomena that interact on multiple scales. This is confirmed by a recent review of intense precipitation events and their large-scale meteorology over North America by Barlow et al. (2019), who concludes that events are often related to mesoscale processes that are triggered, enhanced, or organized by larger-scale processes.

The above examples illustrate that classifying extreme precipitation-producing phenomena is challenging and that scientists might attribute the same event to different phenomena dependent on their data analysis methods. Additionally, manually classifying extreme events is both labor-intensive and time-consuming, and difficult to reproduce. In contrast, automatic algorithms can be very efficient in classifying atmospheric features and allow analyzing vast datasets much more efficiently than manual classification. Automatic algorithms are frequently used to identify atmospheric phenomenon such as tropical cyclones (TC) (Vitart et al., 1997; K. Hodges et al., 2017; Ullrich et al., 2021), extratropical cyclones (Neu et al., 2013), frontal zones (Berry et al., 2011), ARs (Guan & Waliser, 2015; Shields et al., 2018), and MCSs (Davis et al., 2009; A. F. Prein et al., 2020; Feng et al., 2021). However, these algorithms can be prone to creating spurious results and results can be sensitive to their classification settings (A. F. Prein et al., 2020). To date, most feature classification algorithms have been designed to identify single phenomena, which can lead to similar issues as explained for the manual classification above.

Here we present the Multi Object Analysis of Atmospheric Phenomenon (MOAAP) algorithm that uses a set of nine common atmospheric variables to track MCSs, cyclones, anticyclones, TCs, frontal zones, and ARs. Our goal is to understand the contribution of each phenomenon to mean and extreme precipitation on a close-to-global scale and to highlight interactions of different phenomena in producing extreme precipitation. The paper focuses on the past 20 years because of the availability of global hourly precipitation observations. A climatological dataset of atmospheric phenomena is established that can be used in future model evaluation, climate variability, and climate change assessments. All of the identified phenomena have multiple classification criteria in existing literature, which introduces epistemic uncertainty in our analyses. Where possible, we compare our results with published references and discuss potential sources of differences. We select classification criteria based on previously published literature and, where necessary, develop new criteria that reduce the input data demand while reproducing similar statistics. We acknowledge that there are other potentially important phenomena such as stationary thunderstorms, tropical waves, or jet-stream patterns that can cause extreme precipitation events. These are not included in this analysis due to the lack of observational data and our study's objective to minimize the data requirements.

2 Data and Methods

A guiding principle of our approach is to use a minimum set of variables to identify and track a maximum number of atmospheric phenomena. We only use standard output variables that are commonly available from reanalyses and climate models. The following section introduces the selected variables and the methods used for the feature classification.

2.1 Data

We use hourly global or almost global datasets to identify and track features within the period from January 2000 to December 2020. In doing so, we combine variables from the fifth generation reanalysis from the European Centre for Medium-Range Weather Forecasts (ERA5) (Hersbach et al., 2020), NASA global precipitation measurement (GPM) integrated multi-satellite retrievals for GPM (IMERG) (G. J. Huffman, Bolvin, Braithwaite, et al., 2015), and National Oceanic and Atmospheric Administration (NOAA) merged geostationary brightness temperature observations (GPM_MERGIR) (Janowiak et al., 2017).

ERA5 is a state-of-the-art reanalysis product that assimilates a large variety of in-situ and remote-sensing observations into the global Integrated Forecast System (IFS) model to create hourly estimates of the state of the atmosphere within the period 1950 to present on a 30 km grid (Hersbach et al., 2020). The following six variables are used in our analysis: pressure at sea level, zonal and meridional wind speed at 850 hPa, air temperature at 850 hPa, and eastward and northward integrated water vapor flux (IVT). We decided to not use ERA5 precipitation and longwave outgoing radiation since we found that these fields largely deviated from observational products likely due to the coarse grid spacing and the need to parameterize deep convection in ERA5 (Rasmussen & et al., in review). Blending observational fields with reanalysis fields for the identification of phenomenon did not result in problems likely due to the assimilation of these datasets into the ERA5 system.

Instead of precipitation from ERA5 we use estimates from IMERG version 6 that are available from 2000 to the present on a global 0.1° grid every 30-minutes. Data poleward of ±60° is only partially available for grid cells without snow on the ground. IMERG merges satellite microwave precipitation estimates with satellite infrared observations and precipitation gauge records. Although IMERG has a fairly high spatiotemporal spacing, its effective resolution is several times coarser than its grid spacing (Guilloteau & Foufoula-Georgiou, 2020). We also acknowledge that gridded precipitation datasets may under-represent the most extreme precipitation recorded by gauges. Nonetheless, Feng et al. (2021) show that using IMERG precipitation to track MCSs over the U.S. leads to similar results compared to using hourly stage-IV (Lin & Mitchell, 2005) radar-based precipitation estimates.

For cloud brightness temperature we use observations from GPM_MERGIR that merge a range of European, Japanese, and U.S. geostationary satellites observations onto a 60°S–60°N 4-km grid every 30-minutes starting in 2000 (G. J. Huffman, Bolvin, Nelkin, & Tan, 2015). There are occasionally areas with missing data, particularly in the South Pacific. Areas with missing data are treated as not a number values and no cloud features are identified in these regions. Brightness temperature is typically no standard model output but can be estimated from longwave outgoing radiation at the top of the atmosphere (Yang & Slingo, 2001; Wu & Yan, 2011) , which is widely available.

We calculate hourly precipitation accumulations from IMERG and use GPM_MERGIR observations at the full hour to align their temporal resolution with the one from ERA5. Additionally, we regrid these datasets to the ERA5 grid using bi-linear interpolation. All of the analyses presented in this paper are performed on the 30 km regular grid of ERA5 using hourly data.

2.2 Methods

2.2.1 Identification and Tracking of Objects

Our tracking algorithm is based on the connectedness (i.e., adjacent in space and time) of objects in space and time. It is conceptually similar to the Method for Object-Based Diagnostic Evaluation (MODE) Time Domain (MTD) (Davis et al., 2009; Clark et al., 2014; A. F. Prein et al., 2020) and a further developed version of the python-based MCS tracker used in Poujol et al. (2020) and A. Prein et al. (2021). Our tracker applies the following five steps.

1. A threshold is applied to the three-dimensional (time, latitude, longitude) variable of interest resulting in a binary field where all grid cells that are above/below the threshold are set to one (these are the objects of interest), and all other cells are set to zero. Larger absolute threshold values generally result in fewer, smaller, and more intense objects.
2. The binary field is provided to the python label function of the multidimensional image processing tool (ndimage), which is part of the SciPy package. This function identifies objects that are connected in space and time (horizontally or diag-

onal) and assigns them with a unique label (i.e., index) resulting in a feature matrix.
3. For long-lived objects we apply a merging and splitting function to the feature matrix. This function merges or breaks up objects that are connected in time but not in space. E.g., if two objects merge, the smaller object will end at the previous timestep and will be assimilated into the bigger object. Similarly, when an object splits into two objects the larger of the two objects will continue while the smaller object will be treated as a new feature (see Fig. 1). The merging and splitting function allows to define a temporal threshold that ensures that only longer-lived merged and split objects are relabeled. For instance, we only relabel a split object if it exists for longer than 4-hours.
4. From the entire population of identified objects a subset is selected that fulfills a range of criteria that are specific to the atmospheric phenomena under consideration (see Tabel 1 and the following subsection). All objects already fulfill the intensity criteria because of the thresholding performed in step 1. All phenomena except for fronts have temporal criteria that remove short-lived (typically small) objects from the analysis and some phenomena have a minimum area threshold. Additional criteria such as the geometric criteria for ARs or a minimum latitude to detect fronts are also considered.
5. We calculate object characteristics once all objects that qualify as a specific phenomenon are identified.

2.2.2 Object Characteristics

The calculation of object characteristics allows us to perform statistical analyses by e.g., pooling objects within a region. Characteristics are calculated by using the object label to mask the object from its background field (e.g., AR objects are used to extract IVT data). From this data, we calculate object characteristics for each time step (i.e., hour). Those characteristics include the area, sum (e.g., accumulated precipitation), minimum, mean, maximum, and center of mass. The latter is used to calculate the object speed given by the displacement of the center of mass between two time steps. The object speed can fluctuate largely over time mainly due to the merging and splitting of objects, which can result in large changes in the center of mass from one time step to the next (see Fig. 1). We tested alternative methods to calculate the translation speed of objects such as maximizing the pattern correlation by moving the object from the previous time step spatially over the object of the current time step. While this is computationally much more expensive it does not provide a significant improvement over the center of mass-based method.

2.2.3 Cyclone and Anticyclone Detection

Multiple approaches have been proposed to track cyclones (Neu et al., 2013). Some use minimum thresholds in local gradients (Blender & Schubert, 2000), closed contours, and/or minimum pressure (Bardin & Polonsky, 2005). Also, different variables are used to track cyclones, each having benefits and drawbacks (K. I. Hodges et al., 2003). The most common variables are sea level pressure (SLP), geopotential height at low levels, and vorticity (Neu et al., 2013).

We decided to use SLP for tracking cyclones and anticyclones mostly because of its wide availability as a standard model output. The downside of using SLP is that orographic effects can create artificial gradients that might be identified as phenomena (Simmonds & Murray, 1999). We do not use a closed contour criterion because we want our algorithm to work on regional and global domains. Rather than tracking absolute values of SLP, we track SLP anomalies that are derived in three steps. First, we smooth the original SLP field with a uniform square filter with a length of 100 km. This removes small-scale noise and local orographic effects from the SLP field. Second, we calculate the background SLP environment in which cyclones exist. For this, we use a uniform square filter with a side length of 3,000 km and a temporal extent of 78 hours. In the third and final step, we calculate SLP anomalies by subtracting the background state from the filtered field from step 1. Contiguous areas in the anomaly field that are $\leq$-8 hPa and exist for more than 12 hours are identified as cyclones.

Using the anomaly field for tracking cyclones rather than the absolute SLP field has the benefit of being able to track cyclones at lower latitudes that are typically not very deep, but can be very impactful. Fig. 2b shows a representative example of a cutoff-low that formed in August 2002 over the Gulf of Genoa and tracked north-eastward causing major flooding in the northern Alpine region (such storms are called Vb-cyclones in this region, and are known to cause torrential rain (Messmer et al., 2015)).

Anticyclones can also be detected in the same SLP anomaly field. Anticyclones are contiguous areas of SLP anomalies $\geq$ 6 hPa that exist for at least 12 hours. The settings for calculating SLP anomaly fields and the cyclone and anticyclone anomaly thresholds are based on sensitivity tests and comparisons to existing cyclone tracking studies (not shown).

2.2.4 Tropical Cyclone (TCs)

Since TCs are a sub-set of cyclones, we use additional criteria to differentiate TCs from other cyclones. We optimized these criteria based on a comparison to IBTrACS observations (not shown) (Knapp et al., 2010). These criteria are:

- The cyclone minimum SLP must be $\leq$995 hPa. This ensures that cyclones are sufficiently strong to be considered a TC.
- The TC genesis must be equator-ward of $\pm 35°$ latitude.
- TC cannot exist pole-ward of $\pm 60°$ latitude.
- The TC core must be warmer than the average 850 hPa temperature within the cyclone object. This ensures that the TC has a warm core. Optimally, temperatures at higher atmospheric levels should be used to assess the warm core structure of TCs (4–8 km height (Stern & Nolan, 2012)). Using the 850 hPa temperature is a compromise since we use this field for detecting frontal zones and want to minimize the number of necessary algorithm input variables.
- The minimum temperature with the TC at 850 hPa has to be $\geq$285 K.
- The mean cloud shield brightness temperature (Tb) over the TC object must be $\leq$241 K. This helps to eliminate cyclones that do not produce deep convection.

2.2.5 Atmospheric Fronts

We use the algorithm proposed by Parfitt et al. (2017) for detecting frontal zones. The frontal variable (F^*) is calculated as:

$$F^* = \zeta_p |\nabla(T_p)|, \tag{1}$$

where T is the air temperature at a pressure surface (p; here 850 hPa) and ζ_p is the curl of the wind vector that is normal to the pressure surface. Next, we calculate the non-dimensional and normalized frontal diagnostic F as:

$$F = \frac{F^*}{f|\nabla T|_0}, \tag{2}$$

where f is the Coriolis parameter at the corresponding latitude and $|\nabla T|_0 = 0.45\,\mathrm{K}/100\,\mathrm{km}$. Fronts are identified in grid cells where $F > 1$. An example of frontal zones is shown in brown contours Fig. 2d over Eastern Europe and south of France. A caveat in using this frontal definition is that grid cells close to the equator can not be analyzed since f becomes zero. Additionally, orographic effects on temperature and wind speed frequently introduce stationary fronts over mountain regions (e.g., see Fig. 2f), which complicates the analysis of fronts over areas with steep orographic gradients. We decided to only identify but not track frontal zones since the hourly input data from ERA5 is typically too coarse to connect thin and often fast-moving frontal zones in time.

2.2.6 Mesoscale Convective Systems (MCSs)

We identify mesoscale precipitation areas that include convective precipitation by using hourly GPM-IMERG precipitation on the ERA5 grid. In doing so, we mask all hourly precipitation grid cells with more than $2\,\mathrm{mm\,h^{-1}}$ and select contiguous areas that are $5{,}000\,\mathrm{km^2}$ for at least four hours. We call these features mesoscale precipitation objects.

Additionally, we track mesoscale ice cloud shields similarly to mesoscale precipitation objects. We mask all grid cells in the hourly regridded brightness temperature that have temperatures less than or equal to 241 K. We remove all features that do not have cloud shields $\geq 40{,}000\,^2$ for more than four hours. This or similar thresholds are widely used in identifying MCSs maddox1980mesoscale,feng2021

We define MCSs as a combination of a mesoscale precipitation object under a mesoscale ice cloud shield. However, we need additional criteria to make sure that the precipitation is originating from deep convection. Therefore, we demand a minimum cloud brightness temperature of $\leq$225 K at least once during the MCS lifetime (associated with overshooting cloud tops) and that the maximum hourly precipitation is more than $10\,\mathrm{mm\,h^{-1}}$ during the MCS lifetime. These criteria for MCS detection are similar to previous studies (A. Prein et al., 2021; Feng et al., 2021).

2.2.7 Atmospheric Rivers (ARs)

We use IVT to identify AR objects. ARs must have IVT values of at least $500\,\mathrm{kg\,m^{-1}\,s^{-1}}$ and last at least 9-hours. We decided to use a rather high $500\,\mathrm{kg\,m^{-1}\,s^{-1}}$ threshold since previous work has shown that it results in more reliable results when applied globally (Reid et al., 2020). All objects that fulfill this criterion are called IVT streams. To classify as an AR, IVT streams must be at least 2,000 km long and must be at least twice as long as wide (Neiman et al., 2008; Rutz et al., 2014; Reid et al., 2020; Guan & Waliser, 2015). Additionally, we demand that the centroid of an AR is poleward of 20 °, which helps to eliminate persistent objects in the tropics that would otherwise classify as ARs.

3 Results

3.1 Case Studies of Interacting Phenomena During Extreme Precipitation Events

We illustrate MOAAP's multi-feature identification approach by showing the tracks and atmospheric conditions of three recent and extensively studied extreme precipitation events starting with the U.S. landfall of tropical cyclone Florence in September 2018 (Fig. 2a,b). The track of the TC is very similar to the track of its associated precipitation, cloud shield, and IVT stream objects (Fig. 2a). During landfall (Fig. 2b), Florence was fully wrapped within an IVT stream object meaning that it transported a large amount of moisture around its center. We can also detect frontal objects around the center of the TC indicating strong gradients in temperature and pressure. Importantly, an anticyclone object is detected northeast of Florence, which helped stall the system during landfall causing catastrophic flooding.

As a second example, we selected the northern Alpine flooding of August 2002 where a cutoff low developed over the Gulf of Genoa and slowly tracked northeastward producing large rainfall amounts (Fig. 2c,d). Cyclones with these tracks are known flood producers in this region and are called Vb-cyclones (Bebber, 1882; Hofstätter et al., 2018). The track of the cyclone, the cloud shield, the precipitation object, and the IVT stream develop in parallel at the beginning of the event and then start to deviate as the storm moves northeastward and weakens. The IVT stream object indicates the advection of moist air from the Mediterranean but in comparison to Florence, this storm is weaker and is not able to wrap the IVT object around its core. Anticyclones to the west, south, and east contributed to the slow movement speed of this cyclone.

The last example is an AR event that contributed to major flooding in California in January 2017. We can track the IVT stream and associated cloud shield from the middle of the North Pacific to landfall and beyond (Fig. 2e). The associated cyclone is fairly stationary and sometimes connects to a cyclone in the east resulting in a convoluted track. At landfall, the moisture flux towards the U.S. West Coast is amplified by a cyclone in the north and an anticyclone in the south. We will see later that this general pattern of an anticyclone, AR, cyclone (from south to north) is common during the landfall of heavily precipitating ARs.

3.2 Scale Analysis of Atmospheric Phenomena

Scale diagrams that visualize the time and spatial scale of various atmospheric phenomena, such as shown in Kotamarthi et al. (2016) (see their Fig. 7), are useful to understand the spatiotemporal characteristics of motions in the atmosphere. Such diagrams are typically based on expert knowledge. Fig. 3 shows a fully data-driven version of a scale diagram based on the tracking results in this study. We can sample meso-alpha to macro-alpha scales (Orlanski, 1975) and hours to weeks since ERA5 has a horizontal grid spacing of $\sim$30 km, hourly output, and we are tracking phenomena one month at a time, meaning that phenomena that life from one month to the next are split into two. While this increases the frequency of phenomena and reduces their duration, it has little effect on the overall statistics since most phenomena live much shorter than a month. We calculate the length scale of each phenomenon from its area by assuming circular shapes. MCSs are with an average lifetime of $\sim$10 hours and an average length of $\sim$200 km the smallest phenomena that we track while ARs are with 1,000 km and $\sim$2.7 days the largest and longest-lived. This is partly related to the criteria that ARs have to be at least 2,000 km long. Cyclones and anticyclones occupy a wide range of length scales with anticyclones typically being shorter-lived than cyclones. Large cyclones and anticyclones often occur in mid-latitudes while their polar counterparts are typically much smaller (not shown). TCs have similar average lifetimes as cyclones but have larger average length scales. There is a tendency that larger objects are also longer-lived. Generally, these results agree with expectations but the significant amount of overlap between the spatiotemporal space that different phenomena occupy is often misrepresented in existing scale diagrams.

3.3 Climatology of Atmospheric Phenomena

Fig. 4 shows the climatological frequency of phenomena and their month of peak occurrence. These frequencies represent the average number of days that a grid cell is occupied by a phenomenon. Note that this is not the track density but incorporates the phenomenon's spatial extent. Seasonal feature frequencies are shown in supplementary Fig. S1.

Cyclones feature a global hot spot of up to 200 days per year in the Southern Ocean around 60 °S and 120 °E (Fig. 4a). The northern hemisphere features the well known storm tracks in the North Pacific and North Atlantic. Cyclone frequencies typically peak in winter meaning during DJF in the northern hemisphere and JJA in the southern hemisphere (Fig. 4b). However, there are some noticeable exceptions such as an April peak of cyclones in the western and central U.S. or over northeast Asia. The spatial pattern of cyclone frequencies agrees well with previous studies (Neu et al., 2013; Ullrich & Zarzycki, 2017) but the absolute values are hard to compare since most studies present track densities instead of object frequencies. We believe showing the latter is more informative since it better represents the impact of a phenomenon on an area that can extend large distances from its center.

Anticyclones feature maxima north and south of the area of maximum cyclone frequency in both hemispheres (Fig. 4c). A band of high anticyclonic activity spans across the southern hemisphere at $\sim$40 °S, which persists through all seasons and migrates northward during JJA (Fig. 4d). There is also a high frequency of anticyclones over Antarctica. Over the northern hemisphere, anticyclone frequencies are highest in DJF and lowest in JJA with local maxima over the eastern parts of the Pacific and Atlantic basin, and the Beaufort Sea. Further hotspots exist over central Asia and Greenland that should be interpreted with caution since they are partly a result of interpolating surface pressure to sea level. These frequency patterns agree well with previously published data (Pepler et al., 2019).

AR frequencies show maxima over all mid-latitude ocean basins (Fig. 4e), and have a characteristic diagonal orientation (equator-ward in the west and pole-ward in the east) that is associated with hot spots in cyclones and anticyclones. ARs occur most frequently between these two hot spot regions and reach their peak frequency during JFM in most areas of the southern hemisphere while a clear seasonal progression is visible in the north-east Pacific and north-east Atlantic (Fig. 4f). Here, northern regions have a late summer peak changing to a winter peak in southern regions.

Our front detection algorithm frequently identifies stationary fronts over regions with steep topography (Fig. 4g). This is likely the reason why Parfitt et al. (2017), whose algorithm we apply, only showed results over ocean regions. Regions with the highest frontal activity are close to the east coasts in northern mid-latitudes. No prominent hotspots are visible over the southern hemisphere except for subtropical areas west of South America and Africa and coastal regions around Antarctica. Frontal statistics in the latter area are likely affected by strong land-ocean and orographic gradients. These general patterns agree well with results shown in Berry et al. (2011) and Parfitt et al. (2017) except for the hotspots in the subtropical southern Pacific and Atlantic. Fronts are most frequent during DJF over oceans in the northern hemisphere, while land regions frequently feature a spring peak (Fig. 4h). Over the southern hemisphere, fronts are most frequent during JJA.

MCSs are most common in the Intertropical Convergence Zone (ITCZ), particularly over the warm pool region, over the Amazon basin, and the Congo basin (Fig. 4i). In mid-latitudes, the La Plata basin and the Southeastern U.S. feature the highest activities. The different mechanisms that cause MCSs are visible in their seasonality (Fig. 4j). The northward and southward propagation of the ITCZ is visible in the tropical Atlantic and Pacific. Mid-latitude ocean regions feature winter-time maxima while mid-latitude land areas deviate from this pattern and show spring and summer peak frequencies.

TCs occur over sub-tropical and mid-latitude ocean regions with a global hotspot in the west Pacific (Fig. 4k). Our algorithm erroneously picks up TCs in the South Atlantic, which is similar to Ullrich et al. (2021) and might partly be related to using ERA5 data for TC identification. The seasonal peak months of TCs are late summer and early fall in both hemispheres (Fig. 4l).

3.4 Phenomena Contribution to Mean and Heavy Precipitation

In this subsection, we discuss the fractional contribution of each phenomenon's precipitation to total annual precipitation and how frequently each phenomenon contributes to the top 99th percentile hourly precipitation events at each grid cell (Fig. 5). We incorporate the precipitation within each object's extent and the precipitation under mesoscale ice cloud shields that are intersecting with the phenomenon. E.g., for TCs we account for the precipitation in the area of the low-pressure anomaly and the precipitation in the adjacent ice cloud shield.

Commonly we do not associate anticyclones with precipitation and this is true for their core regions but precipitation frequently originates across their pole-ward flanks such as shown for the land-falling AR in Fig. 2f. This most often happens in the South Atlantic where some regions experience more than 40 % of their annual rainfalls in the vicinity of anticyclones (Fig. 5a). In the northern hemisphere, the Karakoram region is the hot spot for precipitation under anticyclonic influence, which is related to the frequently detected anticyclones over steep topography partly originating from extrapolating surface pressure from high altitudes to mean sea level. Concerning extreme precipitation, anticyclones can play an important role in mid-latitude ocean basins, particularly in the South Atlantic and parts of the South Indian Ocean (Fig. 5b).

Cyclonic rainfall contributions are shifted poleward from those of anticyclones (Fig. 5c). The Northeast Atlantic is the global hotspot for cyclonic precipitation with more than 50 % of the annual rainfall related to cyclonic activity. Other regions with more than 40 % cyclonic precipitation are in the Northeast and Northwest Pacific, the South Atlantic, and the Southern Indian Ocean. All ocean regions pole-ward of $\pm 30°$, except for the southeast Pacific, receive more than 50 % (with peaks of more than 90 %) of their hourly heavy precipitation from cyclones. The West Coast and eastern part of North America, parts of Europe, Japan, and parts of central Asia are land hotspots for heavy cyclonic precipitation (Fig. 5c).

TCs are a very small subset of cyclones that contribute little to total precipitation except for a small area in the West Pacific that gets more than 20 % of its annual rainfall from TCs (Fig. 5e). The values presented here are smaller than in previous studies – e.g., by Rodgers et al. (2001) or Jiang and Zipser (2010), compare to their Fig. 5d). This has two reasons. First, we systematically under-count TC frequencies in areas that Jiang and Zipser (2010) identified as hot spots such as the Northeast and Northwest Pacific, and second, rather than using a fixed radius around the center of a TC (typically $\sim$500 km is used), we account for precipitation in the TC object (low-pressure anomaly, see Fig.2b) and precipitation underneath the TC cloud shield. The latter will result in not accounting for TC precipitation in remote cloud bands that are not directly connected to the system. TC contributions to extreme hourly rainfall can reach up to 50 % in the Northwest Pacific but are low otherwise (Fig. 5f). This low contribution of TCs to extreme hourly rainfall might be surprising but it is predominantly due to their rarity and their relative contribution to extremes is higher when investigating rarer (more intense) extreme precipitation events as we will show later.

Precipitation from AR accounts for more than 50 % of annual precipitation over the central regions of mid-latitude ocean basins. There is little AR rainfall contribution over land except for islands and coastal areas (Fig. 5e). The magnitude and location where ARs contribute to heavy rainfall are similar to those of CY (except over land), which is not surprising since those two phenomena are closely linked (e.g., see Fig. 2c). Our results agree well with previous analyses and highlight similar hot spot regions of extreme precipitation contributions from ARs (Waliser & Guan, 2017).

MCSs contribute the majority of precipitation in the tropics and some mid-latitude land regions such as Southeast South America and the Central U.S., which is in good agreement with published literature (Nesbitt et al., 2006; Feng et al., 2021) (Fig. 5g). Even higher contributions of MCSs are found for extreme hourly precipitation with rates of more than 80 % in the tropics, subtropics, the eastern U.S., large parts of Sub-Saharan Africa, South America, and China (Fig. 5h).

3.5 Phenomena Related to Extreme Precipitation Events

Here we investigate what phenomena were present in a 1,000 km radius around the top 100 heaviest hourly precipitation events in each IPCC AR6 region (Iturbide et al., 2020). Note that this method results in selecting much rarer events compared to using the 99th percentile of hourly rainfall in each grid cell used in the previous section.

Fig. 7 shows that interactions between phenomena during extreme hourly precipitation events are the norm and not the exception in most regions. For instance, the Eastern North America (ENA) region gets all of its top 100 hourly extreme rainfall events from MCSs, 70 % of them are near a front, ∼50 % are in the vicinity of a cyclone, ∼40 % are near an anticyclone or AR, and 10 events are related to a TC. Most tropical regions get the majority of their extreme hourly precipitation events from MCSs while cyclones become dominant in higher latitudes. ARs are major contributors to hourly extreme precipitation events on the west coast of North America (WNA and NWN region; Waliser and Guan (2017)) northern Europe (NEU; Lavers and Villarini (2013)), southern South America (SSA; Viale et al. (2018)), New Zealand (NZ; Reid et al. (2021)), and the south Atlantic Ocean. Surprising is the frequent presence of anticyclones in the vicinity of extreme precipitation in mid and high latitudes.

We find similar results when considering the top 100 daily extreme precipitation events (see supplementary Fig. S2). Noteworthy differences include the higher contribution of TCs to daily compared to hourly events in regions around the northwest and the southwest Pacific Ocean, and the much larger contribution from CY in central and eastern North America, and Southeast South America. These differences are likely caused by the increasing importance of rainfall duration for daily extreme events compared to hourly extremes. TCs and CY have much longer lifetimes than MCSs (see Fig. 3) and can therefore create longer duration rainfall and higher daily accumulations when storm motion slows.

The contribution of atmospheric phenomenon to extreme precipitation is a function of the rarity of extreme events. Fig. 8 shows the relative contribution of each phenomena to extreme hourly precipitation as a function of event intensity (e.g., the 10th event includes the top 10 most intense precipitation events). For instance, in South Eastern South America (SES) MCSs in combination with fronts and anticyclones were present in the most intense precipitation events while weaker events are more frequently influenced by CY and ARs. In Northern Australia (NAU), East Asia (EAS), and eastern North America (ENA) TCs are gaining in importance with increasing event rarity. Supplementary Fig. S3 shows the same statistics for daily precipitation extremes. While differences depend on the region, there is a tendency of stronger cyclonic influence during the rarest daily extreme events compared to hourly events in many regions.

To better understand which phenomena combinations are interacting during extreme precipitation events we show the frequency of phenomena co-occurrences in Fig. 9. The fewest interactions are found in tropical ocean regions where stand-alone MCSs are the most common source of extreme events. However, MCSs combined with frontal zones are also common. Mid-latitude regions show more complex interactions. For instance, west-central Europe (WCE) features frequent interactions between anticyclones, CY, and fronts. AR-related extreme precipitation events are frequently co-occurring with a pair of CY and anticyclones as visible in the example in Fig. 2. Generally, the combined occurrence of CY and anticyclones is a common feature in many mid-latitude regions during extreme events. Results for daily extreme events are similar (Supplementary Fig. S4) with the most noticeable differences in mid-latitudes where interactions with cyclones increase in importance, and in northern high-latitudes where phenomena interactions decrease in general.

4 Summary and Discussion

In this study, we present the Multi Object Analysis of Atmospheric Phenomenon (MOAAP) algorithm to identify extratropical and tropical cyclones, anticyclones, ARs, MCSs, and frontal zones and applied it to historical data to better understand how these features are related to mean and extreme precipitation on a global scale. The main advantage of using a multi-feature-based approach compared to single-feature-based methods that are most common in the existing literature is that it allows us to study interactions between phenomena in extreme precipitation-producing environments. Such interactions are known to be important (Barlow et al., 2019) but are understudied systematically on a global scale.

Many approaches exist in the published literature to identify and track individual phenomena such as TC, cyclones, or ARs. Where available, we established methods to maximize the quality of the phenomenon classification. We alsominimized the amount of input data, and used variables that are standard model outputs. The main results and conclusions from this study are:

- Extreme hourly and daily precipitation events are typically caused by multiple atmospheric phenomena that interact on different scales and maximize local precipitation rates. This is intuitive since the need for the alignment and interaction of multiple phenomena is the prime reason why those events are rare and agrees with previous studies over North America (Barlow et al., 2019). Therefore, associating extreme precipitation events to a single atmospheric process can be misleading and often oversimplifies the multi-scale interactions involved. It is also important to note that the investigated phenomena are not physically or statistically independent of each other (e.g., cyclones typically have frontal systems).
- MCSs dominate the water cycle in the tropics and continental areas of the subtropics such as the Eastern U.S., Southeast South America, and parts of Southern Africa in agreement with previous findings (Nesbitt et al., 2006; Feng et al., 2021). Hourly and daily precipitation extremes are almost exclusively related to MCSs in these regions.
- TCs are a minor contributor to the global water cycle and are of secondary importance for extreme hourly and daily precipitation production. However, this is mainly due to how we define extremes in our analyses and TCs might play a much more significant role in extreme statistics when higher-end extremes would be considered (e.g., the one-in-a-hundred-year event). The advent of such high-resolution climate modeling (Haarsma et al., 2016) and particularly km-scale climate modeling (A. F. Prein et al., 2015; Stevens et al., 2019; Mahoney et al., 2021) could help to alleviate some of the observational record-length issues that limit our understanding of high-impact extreme events.
- At higher latitudes, pairs of cyclones and anticyclones play an important role in extreme precipitation production. The co-occurrence of these two phenomena increases moisture convergence and transport. This is a prime mechanism in regions with strong AR events but also plays an important role in other regions such as in central and Northeastern Asia.

The findings listed above should be interpreted alongside the following caveats related to our approach.

- The frontal detection algorithm often identifies fronts over steep topography and coastlines. This leads to an overestimation of precipitation related to fronts in these regions. Additionally, hourly model output is typically not sufficient to track frontal objects and only allowes us to study them as 2D features.
- The TC tracking algorithm could be improved, particularly in the South Atlantic and South Pacific basins. Identifying warm cores at higher tropospheric levels would be beneficial but would increase the input data volume.
- The thresholds to identify phenomena (see Table 1) could be scale dependent and might have to be re-tuned particularly when applied to much coarser resolution data (i.e., one degree or larger). The thresholds can be easily changed in the MOAAP algorithm to optimize it to various input datasets.
- IMERG precipitation does not cover high latitudes and smooths out hourly precipitation features (Guilloteau & Foufoula-Georgiou, 2020). Additionally, deficiencies have been reported over mountain regions (Bartsotas et al., 2018; G. Huffman, 2019). The results presented here should, therefore, be interpreted with caution over high-mountain and high-latitude regions.

Future work will focus on addressing these caveats. Additionally, MOAAP will be applied as a lagrangian evaluation tool to global and regional climate model simulations and to improve our understanding of climate change impacts on the occurrence of phenomena, phenomena characteristics, and their relation to mean and extreme precipitation. Adding additional phenomena such as jet streams or smaller scale convection and phenomena in the land surface or ocean could provide further insights into the physical processes contributing to extreme precipitation, particularly in phenomena interactions in the coupled earth system. Finally, the results from this feature-based analysis could be used to train machine learning algorithms, most of which currently rely on labeling features by hand (Kashinath et al., 2021).

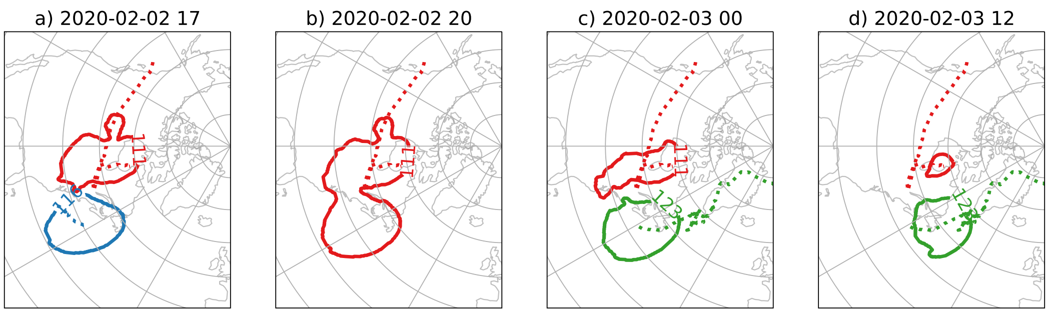

Figure 1. Example for merging and tracking of cyclones over eastern North America. Cyclone number 111 (red) and 110 (blue) collide on Feb. 2, 2020 (a) resulting in the termination of the smaller cyclone (110, b). Six hours later, cyclone 111 splits into two cyclones resulting in the genesis of a new cyclone (123, c). Dotted lines show the track of each cyclone. Cyclone 111 ends over Hudson Bay and cyclone 123 moves over Greenland and enters the Arctic Ocean (d).

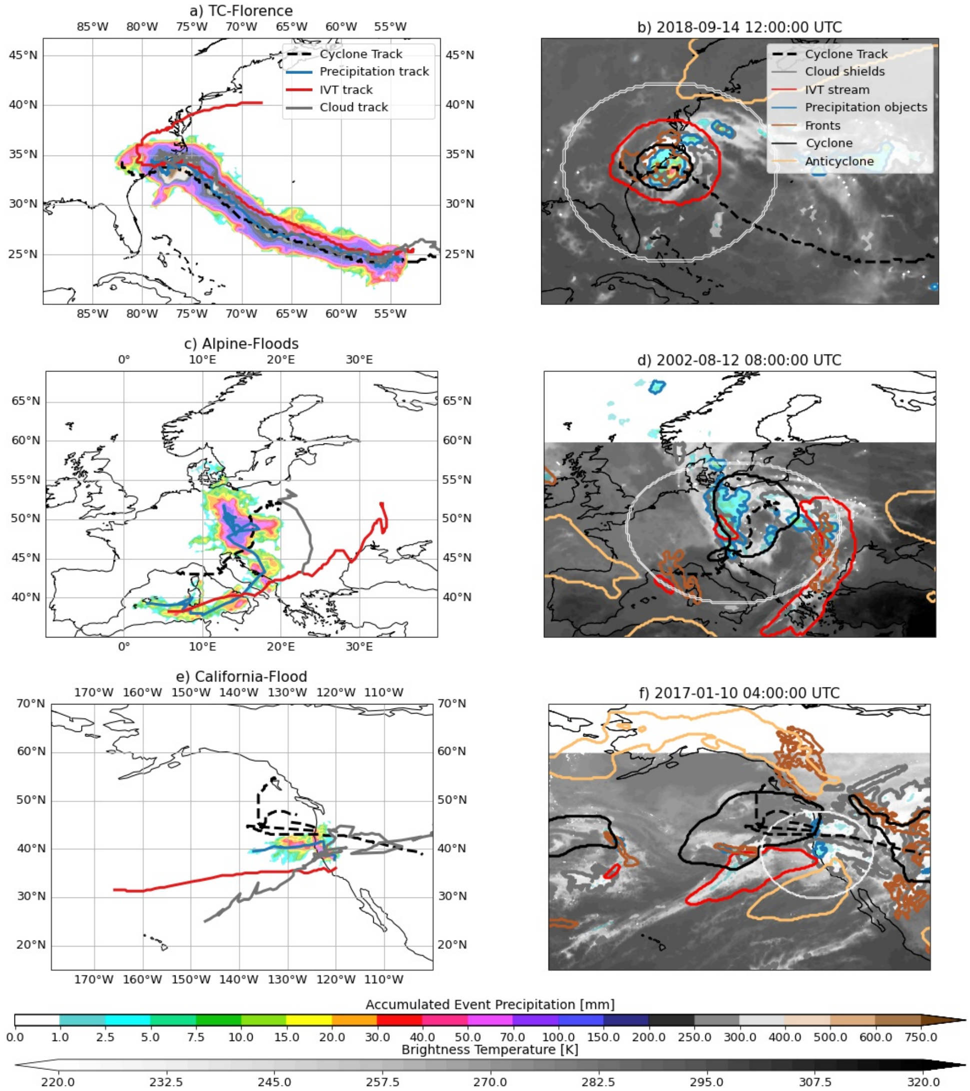

Figure 2. Involved features during the extreme precipitation related to tropical cyclone (TC) Florence in 2018 (a,b), the 2003 Northern Alpine floods (c,d), and the AR event that contributed to the floods in California in early 2017. Colored-filled contours in the left panels show accumulated precipitation from the precipitation feature that resulted in severe flooding. Additionally, the track of involved cyclones (dashed black line), IVT streams (red line), cold cloud tops (grey lines), and the precipitation object (blue line) are shown. The right panels show a snap-shot of the synoptic situation during the flood events with satellite brightness temperature (gray contours), the cyclone track (dashed black line), the outline of the cyclone object (black contour), the IVT object (red contour), cold cloud objects (gray contour), anticyclones (light brown contours), and frontal zones (dark brown). The white circle indicated the 1,000 km search radius that is used to associate phenomena to extreme rainfall events.

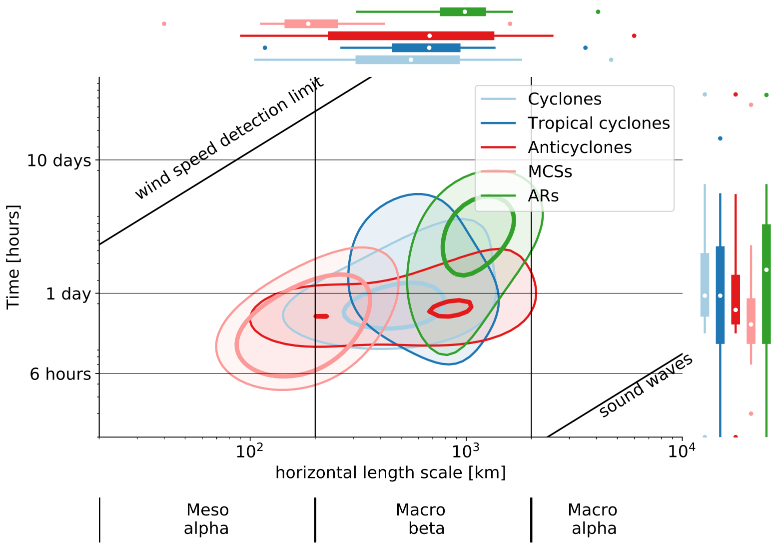

Figure 3. Characteristic feature horizontal length scale (x-axis) and time scale (y-axis) for cyclones (light blue), tropical cyclones (dark clue), MCSs (light red), anticyclones (dark red), and ARs (green). The contours show 2-dimensional Gaussian kernel density estimates with a bandwidth of 0.4 that was applied to the logarithm of the data. The box-whisker plots show the median (white dot), interquartile range (boxes), 5th to 95th percentile (whiskers), and maximum and minimum (colored circles).

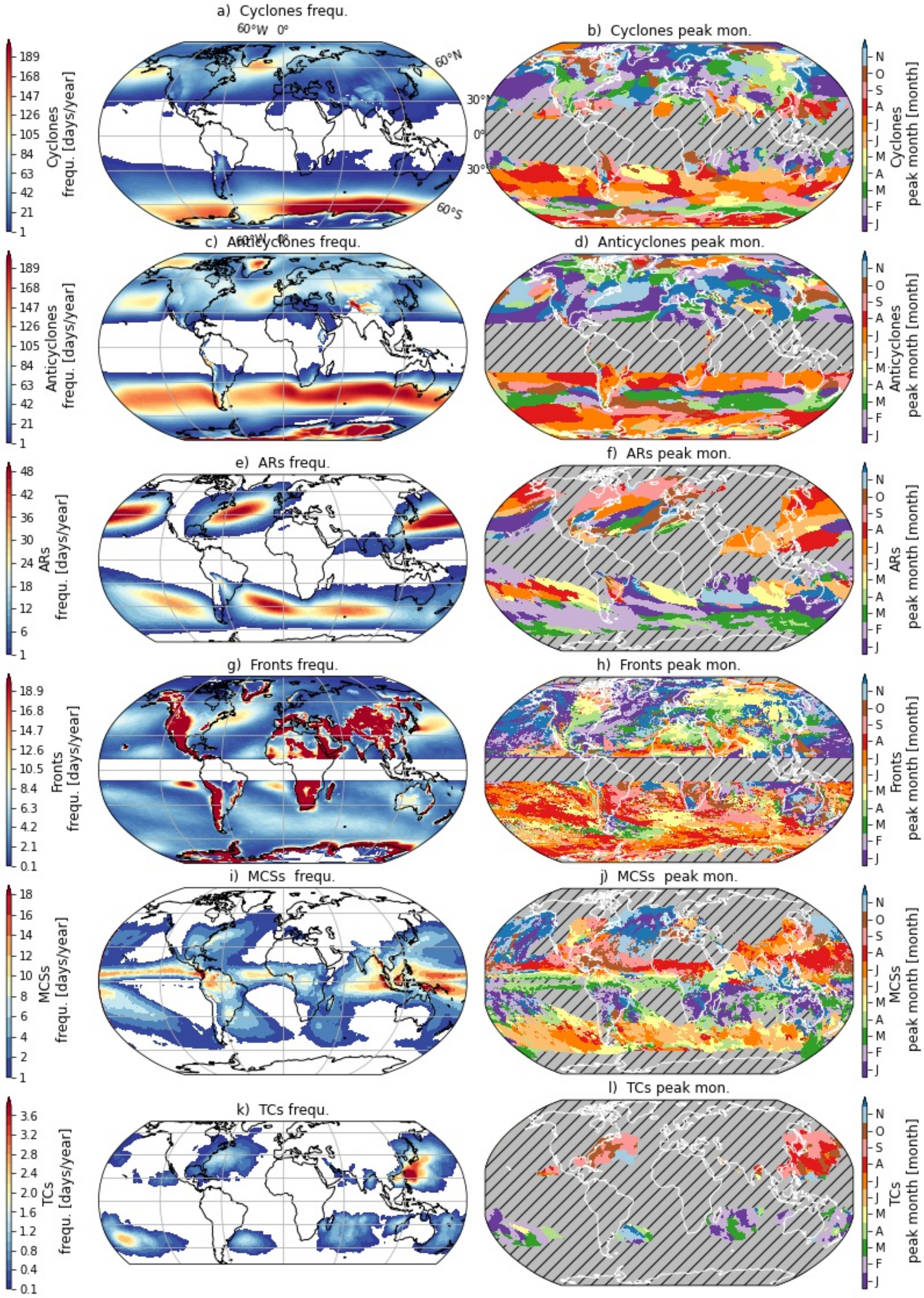

Figure 4. Annual frequency of cyclones, anticyclones, ARs, fronts, MCSs, and TCs features are shown top-down in the left column. The right column shows the color-coded month with their maximum frequency.

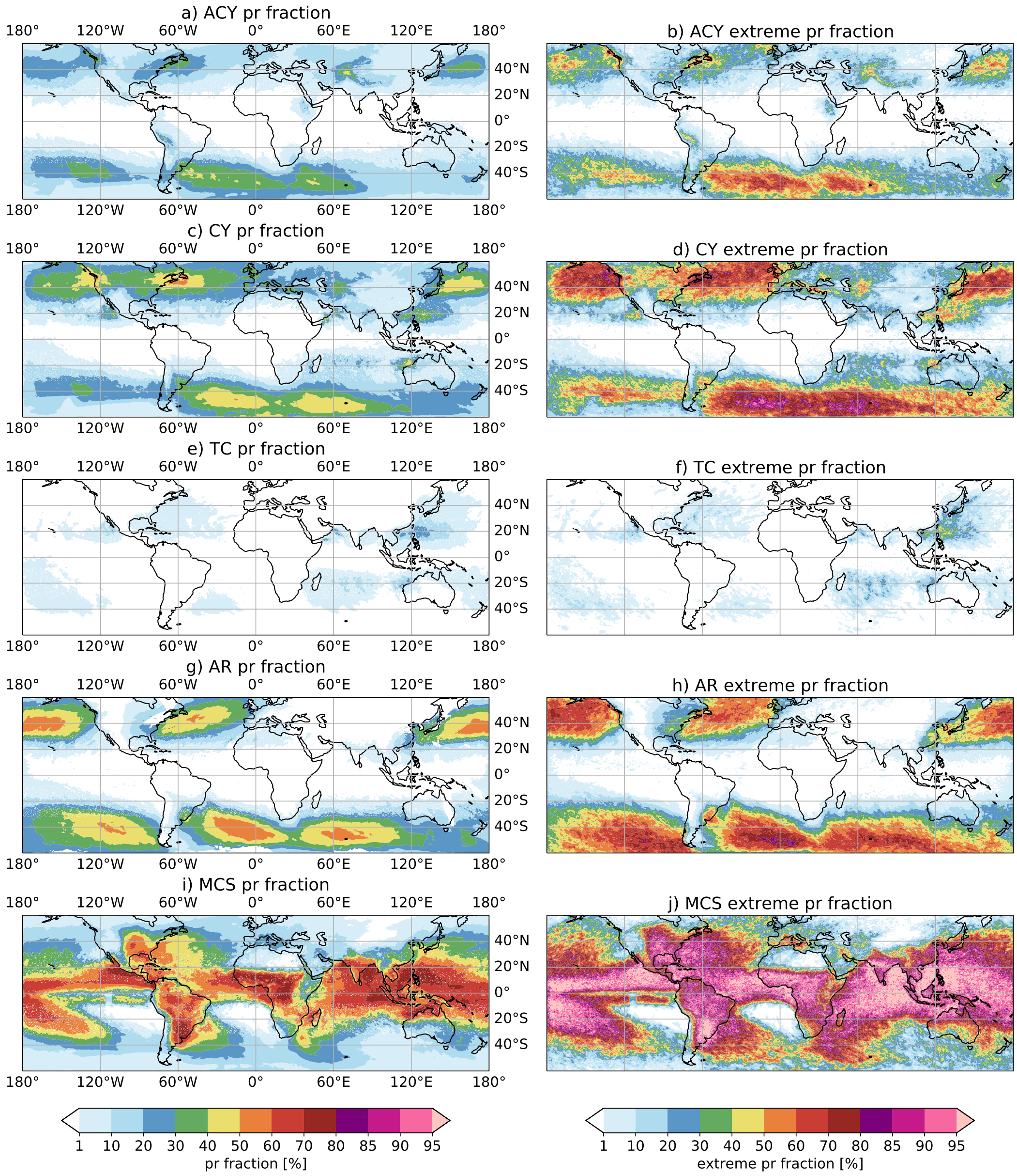

Figure 5. Fraction of precipitation from anticyclones, cyclones, TCs, ARs, and MCSs (top-down) to total precipitation (left column) and the fraction of 99th percentile hourly precipitation event occurrence from each phenomenon (right column).

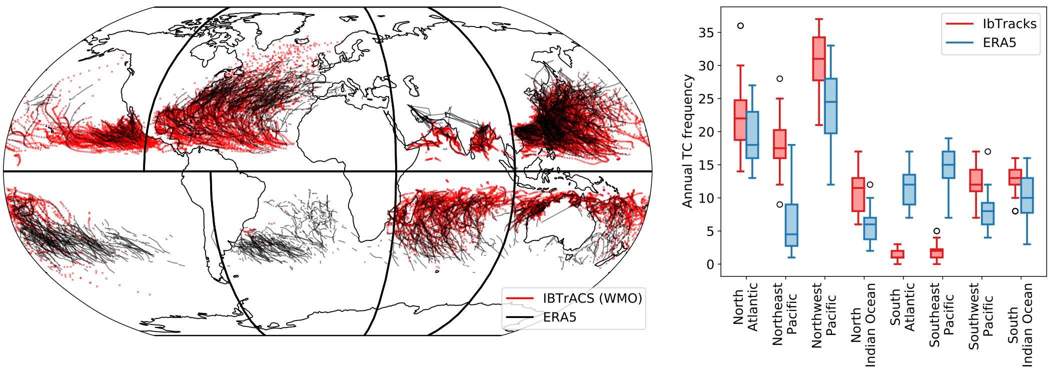

Figure 6. Tropical cyclone tracks from the IBTrACS WMO (red) and our results from tracking TCs in ERA5 (black) over the period 2001–2020 (left). Only category 1 or stronger tropical cyclones on the Saffir-Simpson scale are shown. Annual frequency of TCs in each major ocean basis (right). Box-whisker statistics show the inter-annual variability.

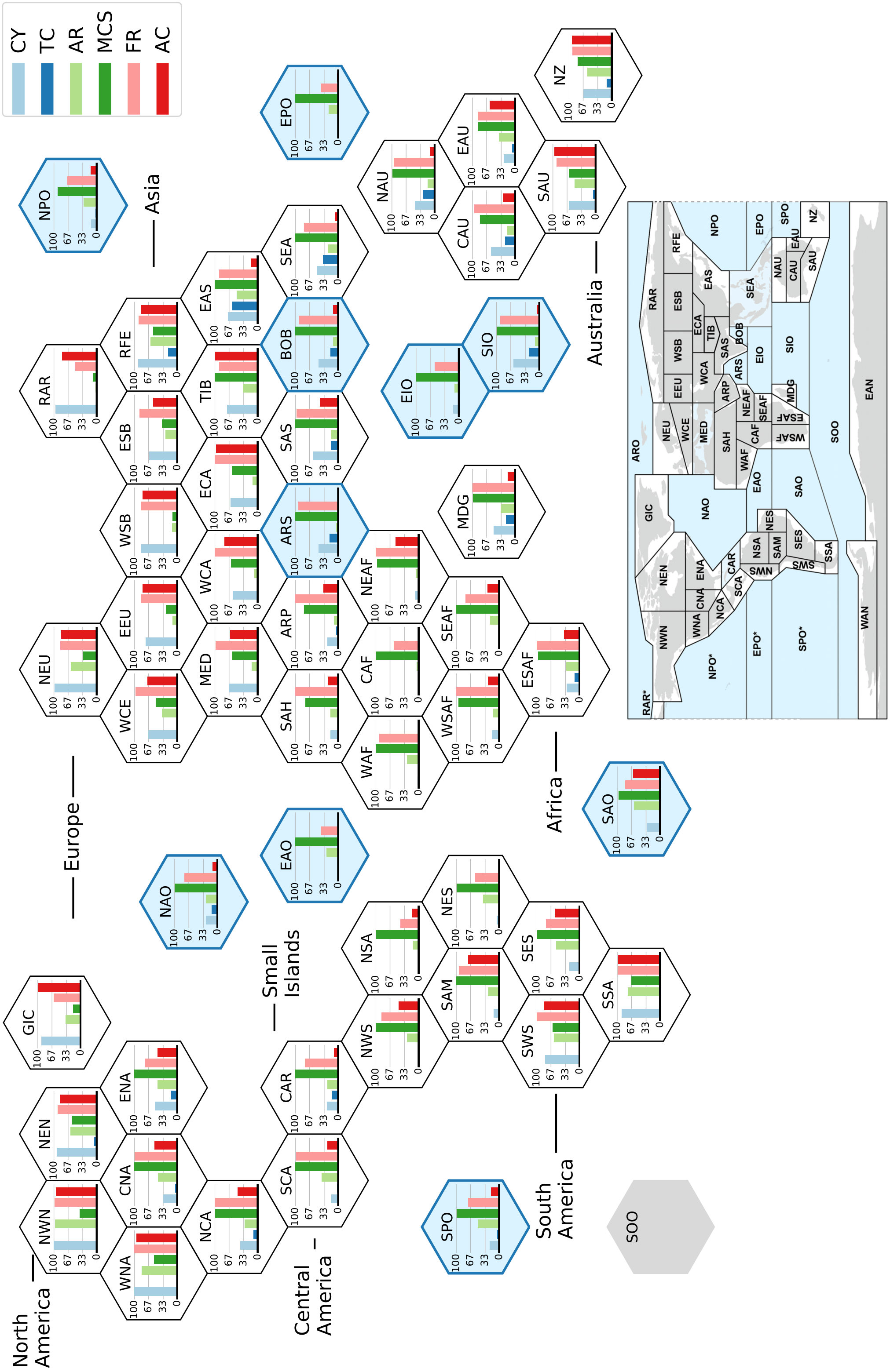

Figure 7. Frequency of features in the vicinity (1,000 km radius) of extreme precipitation events in IPCC AR6 regions. We consider the 100 most extreme hourly precipitation events in each region based on GPM-IMERG precipitation. Blue hexagons indicate ocean regions and grey hexagons do not contain GPM-IMERG precipitation data. The location of each region is shown in the map-inlet in the lower right corner (taken from Iturbide et al. (2020)).

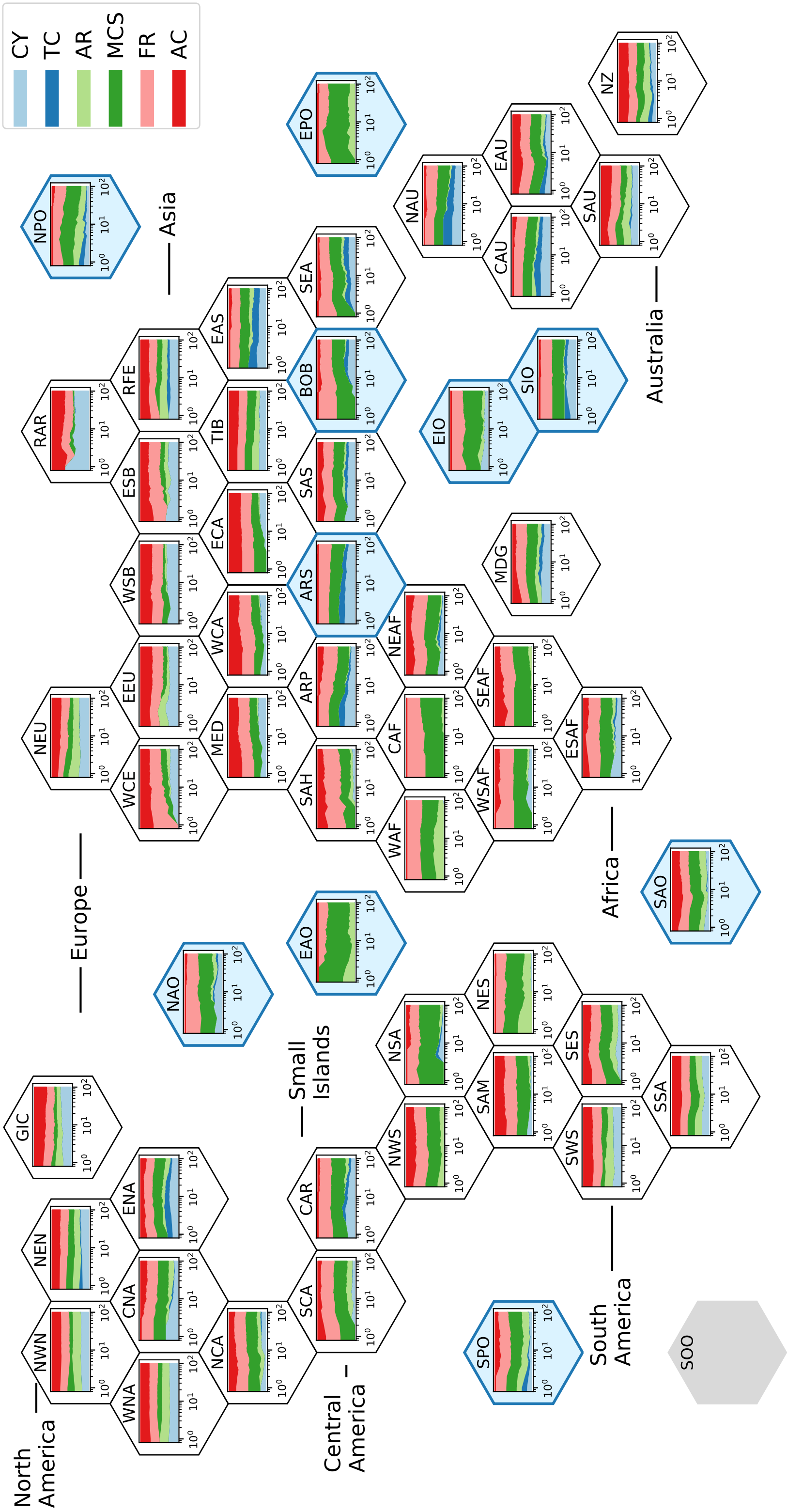

Figure 8. As Fig. 7 but showing the percent contribution (vertical axis) of atmospheric features dependent on the intensity of the extreme precipitation events with the rarest event on the left and all of the 100 most extreme precipitation events on the right.

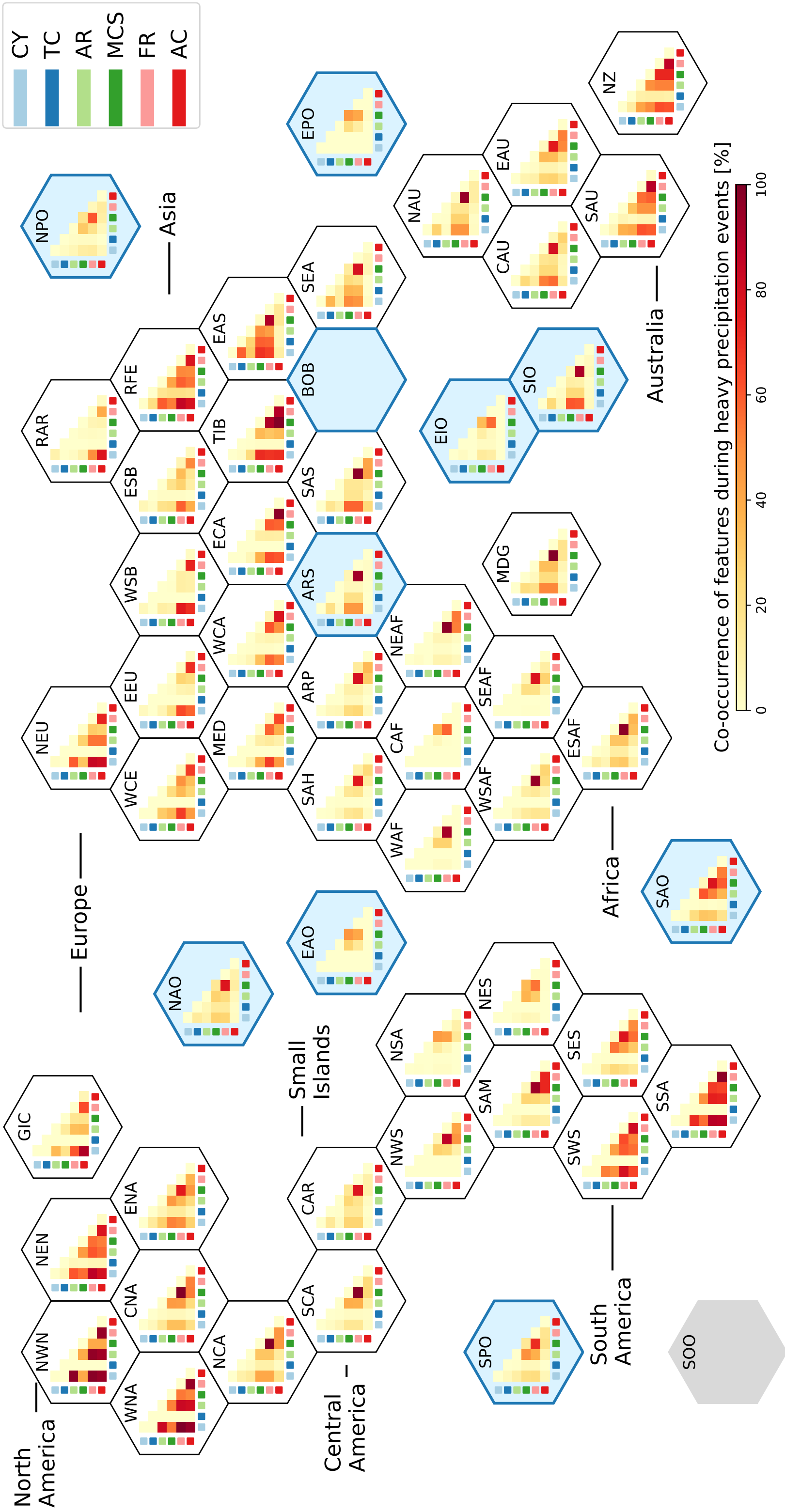

Figure 9. Showing the same data as in Fig. 7 but highlighting the co-occurrence of features during extreme precipitation events. The colors in the heatmaps show the percent of the time at which features co-occurred. The colors beneath the x- and y-axis show the feature as indicated in the legend.

Table 1. Criteria used for feature classification. The following acronyms are used in the table: pressure (P), moisture stream (MS), integrated vapor transport (IVT), brightness temperature (Tb), temperature (T), area (A), the standard deviation of Gaussian smoother (σ; values in brackets correspond to the time, latitude, and longitude dimension).

Feature	Intensity Thresholds	Temporal	Spatial/Area	Additional Criteria	Breakup
Cyclones	$P_{anom} \leq$ -8 hPa	12-hours			yes
Anticyclones	$P_{anom} \geq 6$ hPa	12-hours			yes
IVT Streams	$MS_{min} \geq 0.13$ g/g×m/s	9-hours	$A_{IVT} \geq 100{,}000\,km^2$		yes
ARs	IVT ≥ 500 kg/ms	9-hours		min. length $\geq 2{,}000$ km; length/width ≥ 2; lat. centroid $\geq \pm 20°$	yes
Mesoscale Cloud Shields	Tb ≤ 241 K	9-hours	σ=[0,1,1]; $A_{CL} \geq 40{,}000\,km^2$		no
Mesoscale Precipitation Areas	PR ≥ 2 mm/h	3-hours	σ=[0,1,1]; A_{PR}=5,000 km2		no
Mesoscale Convective Systems	max. PR≥ 3 mm/h; Tb ≤ 241 K; min Tb ≤ 225 K	3-hours	$A_{PR \geq 2mm/h} \geq 2{,}500\,km^2$; $A_{Tb \geq\ 241\ K} \geq 40{,}000\,km^2$	Must be a mesoscale precipitation area and under a mesoscale cloud shield	no
Tropical Cyclones	$P_{min} \leq 995$ hPa; Tb ≤ 241 K; warm core T850 $\geq 0\,°C$; mean $T_{850hPa} \geq 285$ K			max. lat genesis $\leq \pm 35°$; max. lat $\leq \pm 65°$	no
Fronts			$A_{FR} \geq 50{,}000\,km^2$	lat. $\geq \pm 10°$	no

Acknowledgments

The FRONTIER project has received funding from the Research Council of Norway (project number 301777). NCAR is partly sponsored by the National Science Foundation under the Cooperative Agreement No. 1852977. We would like to acknowledge high-performance computing support from Cheyenne (doi:10.5065/D6RX99HX) provided by NCAR's Computational and Information Systems Laboratory, sponsored by the National Science Foundation.

Open Research

ERA-5 reanalysis data can be accessed from the Copernicus Climate Data Store (Copernicus, 2023). The GPM_MERGIR brightness temperature observations can be downloaded from the NASA server (GPM-MERGIR, 2023) and GPM-IMERG precipitation data can also be accessed from NASA (GPM-IMERG, 2023). The MOAAP code can be downloaded from GitHub (Prein, Andreas F, 2023).

References

Bardin, M. Y., & Polonsky, A. (2005). North Atlantic oscillation and synoptic variability in the European-Atlantic region in winter. *Izvestiya atmospheric and oceanic physics*, *41*(2), 127–136.

Barlow, M., Gutowski, W. J., Gyakum, J. R., Katz, R. W., Lim, Y.-K., Schumacher, R. S., … others (2019). North American extreme precipitation events and related large-scale meteorological patterns: a review of statistical methods, dynamics, modeling, and trends. *Climate Dynamics*, *53*(11), 6835–6875.

Bartsotas, N., Anagnostou, E., Nikolopoulos, E., & Kallos, G. (2018). Investigating satellite precipitation uncertainty over complex terrain. *Journal of Geophysical Research: Atmospheres*, *123*(10), 5346–5359.

Bebber, J. v. (1882). *Typische Witterungserscheinungen* (Tech. Rep.). arch. d. Deutschen Seewarte.

Berry, G., Reeder, M. J., & Jakob, C. (2011). A global climatology of atmospheric fronts. *Geophysical Research Letters*, *38*(4).

Blender, R., & Schubert, M. (2000). Cyclone tracking in different spatial and temporal resolutions. *Monthly Weather Review*, *128*(2), 377–384.

Clark, A. J., Bullock, R. G., Jensen, T. L., Xue, M., & Kong, F. (2014). Application of object-based time-domain diagnostics for tracking precipitation systems in convection-allowing models. *Weather and Forecasting*, *29*(3), 517–542.

Copernicus. (2023). *ERA5 hourly data on single levels from 1979 to present [Dataset].* Retrieved from `https://climate.copernicus.eu/climate-reanalysis` doi: 10.24381/cds.adbb2d47

Davis, C. A., Brown, B. G., Bullock, R., & Halley-Gotway, J. (2009). The method for object-based diagnostic evaluation (MODE) applied to numerical forecasts from the 2005 NSSL/SPC Spring Program. *Weather and Forecasting*, *24*(5), 1252–1267.

Feng, Z., Leung, L. R., Liu, N., Wang, J., Houze Jr, R. A., Li, J., … Guo, J. (2021). A global high-resolution mesoscale convective system database using satellite-derived cloud tops, surface precipitation, and tracking. *Journal of Geophysical Research: Atmospheres*, *126*(8), e2020JD034202.

GPM-IMERG. (2023). *GPM-IMERG half-hourly precipitation retrieval [Dataset].* Retrieved from `https://gpm.nasa.gov/data/imerg`

GPM-MERGIR. (2023). *GPM-IMERG half-hourly brightness temperature observations [Dataset].* Retrieved from `https://disc.gsfc.nasa.gov/datasets/GPM_MERGIR_1/summary`

Guan, B., & Waliser, D. E. (2015). Detection of atmospheric rivers: Evaluation and application of an algorithm for global studies. *Journal of Geophysical Research:*

Atmospheres, *120*(24), 12514–12535.
Guilloteau, C., & Foufoula-Georgiou, E. (2020). Multiscale evaluation of satellite precipitation products: Effective resolution of IMERG. In *Satellite precipitation measurement* (pp. 533–558). Springer.
Haarsma, R. J., Roberts, M. J., Vidale, P. L., Senior, C. A., Bellucci, A., Bao, Q., ... others (2016). High resolution model intercomparison project (HighResMIP v1. 0) for CMIP6. *Geoscientific Model Development*, *9*(11), 4185–4208.
Hersbach, H., Bell, B., Berrisford, P., Hirahara, S., Horányi, A., Muñoz-Sabater, J., ... others (2020). The era5 global reanalysis. *Quarterly Journal of the Royal Meteorological Society*, *146*(730), 1999–2049.
Hodges, K., Cobb, A., & Vidale, P. L. (2017). How well are tropical cyclones represented in reanalysis datasets? *Journal of Climate*, *30*(14), 5243–5264.
Hodges, K. I., Hoskins, B. J., Boyle, J., & Thorncroft, C. (2003). A comparison of recent reanalysis datasets using objective feature tracking: Storm tracks and tropical easterly waves. *Monthly Weather Review*, *131*(9), 2012–2037.
Hofstätter, M., Lexer, A., Homann, M., & Blöschl, G. (2018). Large-scale heavy precipitation over central Europe and the role of atmospheric cyclone track types. *International Journal of Climatology*, *38*, e497–e517.
Huffman, G. (2019). *IMERG V06 quality index.* Retrieved from `https://gpm.nasa.gov/sites/default/files/2020-02/IMERGV06_QI_0.pdf`
Huffman, G. J., Bolvin, D. T., Braithwaite, D., Hsu, K., Joyce, R., Xie, P., & Yoo, S.-H. (2015). NASA global precipitation measurement (GPM) integrated multi-satellite retrievals for GPM (IMERG). *Algorithm Theoretical Basis Document (ATBD) Version*, *4*, 26.
Huffman, G. J., Bolvin, D. T., Nelkin, E. J., & Tan, J. (2015). Integrated Multi-satellitE Retrievals for GPM (IMERG) technical documentation. *Nasa/Gsfc Code*, *612*(47), 2019.
Iturbide, M., Gutiérrez, J. M., Alves, L. M., Bedia, J., Cerezo-Mota, R., Cimadevilla, E., ... others (2020). An update of IPCC climate reference regions for subcontinental analysis of climate model data: definition and aggregated datasets. *Earth System Science Data*, *12*(4), 2959–2970.
Janowiak, J., Joyce, B., & Xie, P. (2017). *Merged IR V1, Edited by Andrey Savtchenko, Greenbelt, MD, Goddard Earth Sciences Data and Information Services Center (GES DISC).* `https://disc.gsfc.nasa.gov/datasets/GPM_MERGIR_1/summary`. (Accessed: 2022-03-15) doi: 10.5067/P4HZB9N27EKU
Jiang, H., & Zipser, E. J. (2010). Contribution of tropical cyclones to the global precipitation from eight seasons of TRMM data: Regional, seasonal, and interannual variations. *Journal of climate*, *23*(6), 1526–1543.
Kashinath, K., Mudigonda, M., Kim, S., Kapp-Schwoerer, L., Graubner, A., Karaismailoglu, E., ... others (2021). ClimateNet: an expert-labeled open dataset and deep learning architecture for enabling high-precision analyses of extreme weather. *Geoscientific Model Development*, *14*(1), 107–124.
Knapp, K. R., Kruk, M. C., Levinson, D. H., Diamond, H. J., & Neumann, C. J. (2010). The international best track archive for climate stewardship (IBTrACS) unifying tropical cyclone data. *Bulletin of the American Meteorological Society*, *91*(3), 363–376.
Kotamarthi, R., Mearns, L., Hayhoe, K., Castro, C. L., & Wuebbles, D. (2016). *Use of climate information for decision-making and impacts research: State of our understanding* (Tech. Rep.). Argonne National Laboratory Argonne United States.
Kunkel, K. E., Easterling, D. R., Kristovich, D. A., Gleason, B., Stoecker, L., & Smith, R. (2012). Meteorological causes of the secular variations in observed extreme precipitation events for the conterminous United States. *Journal of Hydrometeorology*, *13*(3), 1131–1141.

Lavers, D. A., & Villarini, G. (2013). The nexus between atmospheric rivers and extreme precipitation across Europe. *Geophysical Research Letters*, *40*(12), 3259–3264.

Lin, Y., & Mitchell, K. E. (2005). 1.2 the NCEP stage II/IV hourly precipitation analyses: Development and applications. In *Proceedings of the 19th conference hydrology, american meteorological society, san diego, ca, usa* (Vol. 10).

Mahoney, K., McColl, C., Hultstrand, D. M., Kappel, W. D., McCormick, B., & Compo, G. P. (2021). Blasts from the past: Reimagining historical storms with model simulations to modernize dam safety and flood risk assessment. *Bulletin of the American Meteorological Society*, 1–35.

Messmer, M., Gómez-Navarro, J. J., & Raible, C. C. (2015). Climatology of Vb cyclones, physical mechanisms and their impact on extreme precipitation over Central Europe. *Earth system dynamics*, *6*(2), 541–553.

Neiman, P. J., Ralph, F. M., Wick, G. A., Lundquist, J. D., & Dettinger, M. D. (2008). Meteorological characteristics and overland precipitation impacts of atmospheric rivers affecting the West Coast of North America based on eight years of SSM/I satellite observations. *Journal of Hydrometeorology*, *9*(1), 22–47.

Nesbitt, S. W., Cifelli, R., & Rutledge, S. A. (2006). Storm morphology and rainfall characteristics of TRMM precipitation features. *Monthly Weather Review*, *134*(10), 2702–2721.

Neu, U., Akperov, M. G., Bellenbaum, N., Benestad, R., Blender, R., Caballero, R., ... others (2013). IMILAST: A community effort to intercompare extratropical cyclone detection and tracking algorithms. *Bulletin of the American Meteorological Society*, *94*(4), 529–547.

Orlanski, I. (1975). A rational subdivision of scales for atmospheric processes. *Bulletin of the American Meteorological Society*, 527–530.

Parfitt, R., Czaja, A., & Seo, H. (2017). A simple diagnostic for the detection of atmospheric fronts. *Geophysical Research Letters*, *44*(9), 4351–4358.

Pepler, A., Dowdy, A., & Hope, P. (2019). A global climatology of surface anticyclones, their variability, associated drivers and long-term trends. *Climate Dynamics*, *52*(9), 5397–5412.

Poujol, B., Prein, A. F., & Newman, A. J. (2020). Kilometer-scale modeling projects a tripling of Alaskan convective storms in future climate. *Climate Dynamics*, *55*(11), 3543–3564.

Prein, A., Rasmussen, R., Wang, D., & Giangrande, S. (2021). Sensitivity of organized convective storms to model grid spacing in current and future climates. *Philosophical Transactions of the Royal Society A*, *379*(2195), 20190546.

Prein, A. F., Langhans, W., Fosser, G., Ferrone, A., Ban, N., Goergen, K., ... others (2015). A review on regional convection-permitting climate modeling: Demonstrations, prospects, and challenges. *Reviews of geophysics*, *53*(2), 323–361.

Prein, A. F., Liu, C., Ikeda, K., Bullock, R., Rasmussen, R. M., Holland, G. J., & Clark, M. (2020). Simulating North American mesoscale convective systems with a convection-permitting climate model. *Climate Dynamics*, *55*(1), 95–110.

Prein, Andreas F. (2023). *Multi Object Analysis of Atmospheric Phenomenon (MOAAP) [Software]*. Retrieved from `https://github.com/AndreasPrein/MOAAP/tree/V1.0` doi: 10.5281/zenodo.7561616

Rasmussen, R. M., & et al. (in review). The NCAR-USGS 4-km long-term regional hydroclimate reanalysis over the CONUS. *BAMS*.

Reid, K. J., King, A. D., Lane, T. P., & Short, E. (2020). The sensitivity of atmospheric river identification to integrated water vapor transport threshold, resolution, and regridding method. *Journal of Geophysical Research: Atmospheres*, *125*(20), e2020JD032897.

Reid, K. J., Rosier, S. M., Harrington, L. J., King, A. D., & Lane, T. P. (2021). Extreme rainfall in New Zealand and its association with Atmospheric Rivers. *Environmental Research Letters*, *16*(4), 044012.

Rodgers, E. B., Adler, R. F., & Pierce, H. F. (2001). Contribution of tropical cyclones to the North Atlantic climatological rainfall as observed from satellites. *Journal of Applied Meteorology*, *40*(11), 1785–1800.

Rutz, J. J., Steenburgh, W. J., & Ralph, F. M. (2014). Climatological characteristics of atmospheric rivers and their inland penetration over the western United States. *Monthly Weather Review*, *142*(2), 905–921.

Schumacher, R. S., & Johnson, R. H. (2006). Characteristics of US extreme rain events during 1999–2003. *Weather and Forecasting*, *21*(1), 69–85.

Shields, C. A., Rutz, J. J., Leung, L.-Y., Ralph, F. M., Wehner, M., Kawzenuk, B., . . . others (2018). Atmospheric river tracking method intercomparison project (ARTMIP): project goals and experimental design. *Geoscientific Model Development*, *11*(6), 2455–2474.

Simmonds, I., & Murray, R. J. (1999). Southern extratropical cyclone behavior in ECMWF analyses during the FROST special observing periods. *Weather and forecasting*, *14*(6), 878–891.

Stern, D. P., & Nolan, D. S. (2012). On the height of the warm core in tropical cyclones. *Journal of the Atmospheric Sciences*, *69*(5), 1657–1680.

Stevens, B., Satoh, M., Auger, L., Biercamp, J., Bretherton, C. S., Chen, X., . . . others (2019). DYAMOND: the DYnamics of the Atmospheric general circulation Modeled On Non-hydrostatic Domains. *Progress in Earth and Planetary Science*, *6*(1), 1–17.

Ullrich, P. A., & Zarzycki, C. M. (2017). TempestExtremes: A framework for scale-insensitive pointwise feature tracking on unstructured grids. *Geoscientific Model Development*, *10*(3), 1069–1090.

Ullrich, P. A., Zarzycki, C. M., McClenny, E. E., Pinheiro, M. C., Stansfield, A. M., & Reed, K. A. (2021). TempestExtremes v2. 1: a community framework for feature detection, tracking, and analysis in large datasets. *Geoscientific Model Development*, *14*(8), 5023–5048.

Viale, M., Valenzuela, R., Garreaud, R. D., & Ralph, F. M. (2018). Impacts of atmospheric rivers on precipitation in southern South America. *Journal of Hydrometeorology*, *19*(10), 1671–1687.

Vitart, F., Anderson, J., & Stern, W. (1997). Simulation of interannual variability of tropical storm frequency in an ensemble of GCM integrations. *Journal of Climate*, *10*(4), 745–760.

Waliser, D., & Guan, B. (2017). Extreme winds and precipitation during landfall of atmospheric rivers. *Nature Geoscience*, *10*(3), 179–183.

Wu, X., & Yan, J. (2011). Estimating the outgoing longwave radiation from the FY-3B satellite visible infrared radiometer Channel 5 radiance observations. *Chinese Science Bulletin*, *56*(32), 3480–3485.

Yang, G.-Y., & Slingo, J. (2001). The diurnal cycle in the tropics. *Monthly Weather Review*, *129*(4), 784–801.

The Multi-Scale Interactions of Atmospheric Phenomenon in Extreme and Mean Precipitation

Andreas F. Prein[1], Priscilla A. Mooney[2], James M. Done[1]

[1]National Center for Atmospheric Research
[2]NORCE, Bjerknes Centre for Climate Research

Key Points:

- A novel algorithm simultaneously tracks cyclones, anticyclones, MCSs, atmospheric rivers, and fronts.
- Extreme precipitation is typically associated with multiple atmospheric phenomena that interact across scales.
- MCSs are involved in most extreme precipitation events in the tropics and many sub-tropical and mid-latitude regions.

Corresponding author: Andreas F. Prein, `prein@ucar.edu`

Abstract

Globally, extreme precipitation events cause enormous impacts. Climate change increases the frequency and intensity of extreme precipitation, which in combination with rising population enhances exposure to major floods. An improved understanding of the atmospheric processes that cause extreme precipitation events would help to advance predictions and projections of such events. To date, such analyses have typically been performed rather unsystematically and over limited areas (e.g., the U.S.) which has resulted in contradictory findings. Here we present the Multi Object Analysis of Atmospheric Phenomenon (MOAAP) algorithm that uses a set of nine common atmospheric variables to identify and track tropical and extra-tropical cyclones, anticyclones, atmospheric rivers (ARs), mesoscale convective systems (MCSs), and frontal zones. We apply the algorithm to global historical data between 2000 to 2020. We find that MCSs produce the vast majority of extreme precipitation in the tropics and some mid-latitude land regions, while extreme precipitation in mid- and high-latitude ocean and coastal regions are dominated by cyclones and ARs. Importantly, most extreme precipitation events are associated with interacting features across scales that intensify precipitation. These interactions, however, can be a function of the rarity (e.g., return period) of extreme events. The presented methodology and results could have wide-ranging applications including training of machine learning methods, lagrangian-based evaluation of climate models, and process-based understanding of extreme precipitation in a changing climate.

Plain Language Summary

Increases in intense precipitation and faster onsets of droughts are just two of many precipitation related extreme events that worsen under progressive climate change. Surprisingly little is know about the weather systems that are driving these changes in many regions around the world. In order to better predict and prepare for these events, scientists need an improved understanding of the causes of the involved atmospheric processes and their interactions. A new algorithm called the Multi Object Analysis of Atmospheric Phenomenon (MOAAP) has been developed to identify and track different types of weather systems, such as tropical and extra-tropical cyclones, that can lead to extreme precipitation. The algorithm was applied to global weather data from 2000 to 2020. The results showed that certain types of weather systems, such as mesoscale convective systems, are frequently involved in causing the most extreme precipitation. Additionally, the study found that most extreme precipitation events are caused by a combination of different weather systems working together, and that these interactions can vary for very rare and more common extreme events. This research could be useful for improving climate models and understanding how extreme precipitation is likely to change in the future.

1 Introduction

Many studies have examined the atmospheric drivers of intense precipitation. Kunkel et al. (2012) analyzed the drivers of 1-in-5-year occurrence of daily precipitation events in the U.S. during the period 1908–2009 and found that more than 70 % of extreme precipitation in the central U.S. is related to frontal systems and less than 10 % to mesoscale convective systems (MCSs). In similar work, Schumacher and Johnson (2006) found a much greater contribution from MCSs of 75 % of warm-season intense precipitation events in the eastern U.S. This highlights: (i) the difficulty in differentiating the dominant phenomena that cause intense precipitation and (ii) that intense events may be influenced by multiple phenomena that interact on multiple scales. This is confirmed by a recent review of intense precipitation events and their large-scale meteorology over North America by Barlow et al. (2019), who concludes that events are often related to mesoscale processes that are triggered, enhanced, or organized by larger-scale processes.

The above examples illustrate that classifying extreme precipitation-producing phenomena is challenging and that scientists might attribute the same event to different phenomena dependent on their data analysis methods. Additionally, manually classifying extreme events is both labor-intensive and time-consuming, and difficult to reproduce. In contrast, automatic algorithms can be very efficient in classifying atmospheric features and allow analyzing vast datasets much more efficiently than manual classification. Automatic algorithms are frequently used to identify atmospheric phenomenon such as tropical cyclones (TC) (Vitart et al., 1997; K. Hodges et al., 2017; Ullrich et al., 2021), extratropical cyclones (Neu et al., 2013), frontal zones (Berry et al., 2011), ARs (Guan & Waliser, 2015; Shields et al., 2018), and MCSs (Davis et al., 2009; A. F. Prein et al., 2020; Feng et al., 2021). However, these algorithms can be prone to creating spurious results and results can be sensitive to their classification settings (A. F. Prein et al., 2020). To date, most feature classification algorithms have been designed to identify single phenomena, which can lead to similar issues as explained for the manual classification above.

Here we present the Multi Object Analysis of Atmospheric Phenomenon (MOAAP) algorithm that uses a set of nine common atmospheric variables to track MCSs, cyclones, anticyclones, TCs, frontal zones, and ARs. Our goal is to understand the contribution of each phenomenon to mean and extreme precipitation on a close-to-global scale and to highlight interactions of different phenomena in producing extreme precipitation. The paper focuses on the past 20 years because of the availability of global hourly precipitation observations. A climatological dataset of atmospheric phenomena is established that can be used in future model evaluation, climate variability, and climate change assessments. All of the identified phenomena have multiple classification criteria in existing literature, which introduces epistemic uncertainty in our analyses. Where possible, we compare our results with published references and discuss potential sources of differences. We select classification criteria based on previously published literature and, where necessary, develop new criteria that reduce the input data demand while reproducing similar statistics. We acknowledge that there are other potentially important phenomena such as stationary thunderstorms, tropical waves, or jet-stream patterns that can cause extreme precipitation events. These are not included in this analysis due to the lack of observational data and our study's objective to minimize the data requirements.

2 Data and Methods

A guiding principle of our approach is to use a minimum set of variables to identify and track a maximum number of atmospheric phenomena. We only use standard output variables that are commonly available from reanalyses and climate models. The following section introduces the selected variables and the methods used for the feature classification.

2.1 Data

We use hourly global or almost global datasets to identify and track features within the period from January 2000 to December 2020. In doing so, we combine variables from the fifth generation reanalysis from the European Centre for Medium-Range Weather Forecasts (ERA5) (Hersbach et al., 2020), NASA global precipitation measurement (GPM) integrated multi-satellite retrievals for GPM (IMERG) (G. J. Huffman, Bolvin, Braithwaite, et al., 2015), and National Oceanic and Atmospheric Administration (NOAA) merged geostationary brightness temperature observations (GPM_MERGIR) (Janowiak et al., 2017).

ERA5 is a state-of-the-art reanalysis product that assimilates a large variety of in-situ and remote-sensing observations into the global Integrated Forecast System (IFS) model to create hourly estimates of the state of the atmosphere within the period 1950 to present on a 30 km grid (Hersbach et al., 2020). The following six variables are used in our analysis: pressure at sea level, zonal and meridional wind speed at 850 hPa, air temperature at 850 hPa, and eastward and northward integrated water vapor flux (IVT). We decided to not use ERA5 precipitation and longwave outgoing radiation since we found that these fields largely deviated from observational products likely due to the coarse grid spacing and the need to parameterize deep convection in ERA5 (Rasmussen & et al., in review). Blending observational fields with reanalysis fields for the identification of phenomenon did not result in problems likely due to the assimilation of these datasets into the ERA5 system.

Instead of precipitation from ERA5 we use estimates from IMERG version 6 that are available from 2000 to the present on a global 0.1° grid every 30-minutes. Data poleward of ±60° is only partially available for grid cells without snow on the ground. IMERG merges satellite microwave precipitation estimates with satellite infrared observations and precipitation gauge records. Although IMERG has a fairly high spatiotemporal spacing, its effective resolution is several times coarser than its grid spacing (Guilloteau & Foufoula-Georgiou, 2020). We also acknowledge that gridded precipitation datasets may under-represent the most extreme precipitation recorded by gauges. Nonetheless, Feng et al. (2021) show that using IMERG precipitation to track MCSs over the U.S. leads to similar results compared to using hourly stage-IV (Lin & Mitchell, 2005) radar-based precipitation estimates.

For cloud brightness temperature we use observations from GPM_MERGIR that merge a range of European, Japanese, and U.S. geostationary satellites observations onto a 60°S–60°N 4-km grid every 30-minutes starting in 2000 (G. J. Huffman, Bolvin, Nelkin, & Tan, 2015). There are occasionally areas with missing data, particularly in the South Pacific. Areas with missing data are treated as not a number values and no cloud features are identified in these regions. Brightness temperature is typically no standard model output but can be estimated from longwave outgoing radiation at the top of the atmosphere (Yang & Slingo, 2001; Wu & Yan, 2011) , which is widely available.

We calculate hourly precipitation accumulations from IMERG and use GPM_MERGIR observations at the full hour to align their temporal resolution with the one from ERA5. Additionally, we regrid these datasets to the ERA5 grid using bi-linear interpolation. All of the analyses presented in this paper are performed on the 30 km regular grid of ERA5 using hourly data.

2.2 Methods

2.2.1 Identification and Tracking of Objects

Our tracking algorithm is based on the connectedness (i.e., adjacent in space and time) of objects in space and time. It is conceptually similar to the Method for Object-Based Diagnostic Evaluation (MODE) Time Domain (MTD) (Davis et al., 2009; Clark et al., 2014; A. F. Prein et al., 2020) and a further developed version of the python-based MCS tracker used in Poujol et al. (2020) and A. Prein et al. (2021). Our tracker applies the following five steps.

1. A threshold is applied to the three-dimensional (time, latitude, longitude) variable of interest resulting in a binary field where all grid cells that are above/below the threshold are set to one (these are the objects of interest), and all other cells are set to zero. Larger absolute threshold values generally result in fewer, smaller, and more intense objects.
2. The binary field is provided to the python label function of the multidimensional image processing tool (ndimage), which is part of the SciPy package. This function identifies objects that are connected in space and time (horizontally or diag-

onal) and assigns them with a unique label (i.e., index) resulting in a feature matrix.

3. For long-lived objects we apply a merging and splitting function to the feature matrix. This function merges or breaks up objects that are connected in time but not in space. E.g., if two objects merge, the smaller object will end at the previous timestep and will be assimilated into the bigger object. Similarly, when an object splits into two objects the larger of the two objects will continue while the smaller object will be treated as a new feature (see Fig. 1). The merging and splitting function allows to define a temporal threshold that ensures that only longer-lived merged and split objects are relabeled. For instance, we only relabel a split object if it exists for longer than 4-hours.
4. From the entire population of identified objects a subset is selected that fulfills a range of criteria that are specific to the atmospheric phenomena under consideration (see Tabel 1 and the following subsection). All objects already fulfill the intensity criteria because of the thresholding performed in step 1. All phenomena except for fronts have temporal criteria that remove short-lived (typically small) objects from the analysis and some phenomena have a minimum area threshold. Additional criteria such as the geometric criteria for ARs or a minimum latitude to detect fronts are also considered.
5. We calculate object characteristics once all objects that qualify as a specific phenomenon are identified.

2.2.2 Object Characteristics

The calculation of object characteristics allows us to perform statistical analyses by e.g., pooling objects within a region. Characteristics are calculated by using the object label to mask the object from its background field (e.g., AR objects are used to extract IVT data). From this data, we calculate object characteristics for each time step (i.e., hour). Those characteristics include the area, sum (e.g., accumulated precipitation), minimum, mean, maximum, and center of mass. The latter is used to calculate the object speed given by the displacement of the center of mass between two time steps. The object speed can fluctuate largely over time mainly due to the merging and splitting of objects, which can result in large changes in the center of mass from one time step to the next (see Fig. 1). We tested alternative methods to calculate the translation speed of objects such as maximizing the pattern correlation by moving the object from the previous time step spatially over the object of the current time step. While this is computationally much more expensive it does not provide a significant improvement over the center of mass-based method.

2.2.3 Cyclone and Anticyclone Detection

Multiple approaches have been proposed to track cyclones (Neu et al., 2013). Some use minimum thresholds in local gradients (Blender & Schubert, 2000), closed contours, and/or minimum pressure (Bardin & Polonsky, 2005). Also, different variables are used to track cyclones, each having benefits and drawbacks (K. I. Hodges et al., 2003). The most common variables are sea level pressure (SLP), geopotential height at low levels, and vorticity (Neu et al., 2013).

We decided to use SLP for tracking cyclones and anticyclones mostly because of its wide availability as a standard model output. The downside of using SLP is that orographic effects can create artificial gradients that might be identified as phenomena (Simmonds & Murray, 1999). We do not use a closed contour criterion because we want our algorithm to work on regional and global domains. Rather than tracking absolute values of SLP, we track SLP anomalies that are derived in three steps. First, we smooth the original SLP field with a uniform square filter with a length of 100 km. This removes small-scale noise and local orographic effects from the SLP field. Second, we calculate the background SLP environment in which cyclones exist. For this, we use a uniform square filter with a side length of 3,000 km and a temporal extent of 78 hours. In the third and final step, we calculate SLP anomalies by subtracting the background state from the filtered field from step 1. Contiguous areas in the anomaly field that are $\leq$-8 hPa and exist for more than 12 hours are identified as cyclones.

Using the anomaly field for tracking cyclones rather than the absolute SLP field has the benefit of being able to track cyclones at lower latitudes that are typically not very deep, but can be very impactful. Fig. 2b shows a representative example of a cutoff-low that formed in August 2002 over the Gulf of Genoa and tracked north-eastward causing major flooding in the northern Alpine region (such storms are called Vb-cyclones in this region, and are known to cause torrential rain (Messmer et al., 2015)).

Anticyclones can also be detected in the same SLP anomaly field. Anticyclones are contiguous areas of SLP anomalies $\geq$ 6 hPa that exist for at least 12 hours. The settings for calculating SLP anomaly fields and the cyclone and anticyclone anomaly thresholds are based on sensitivity tests and comparisons to existing cyclone tracking studies (not shown).

2.2.4 Tropical Cyclone (TCs)

Since TCs are a sub-set of cyclones, we use additional criteria to differentiate TCs from other cyclones. We optimized these criteria based on a comparison to IBTrACS observations (not shown) (Knapp et al., 2010). These criteria are:

- The cyclone minimum SLP must be $\leq$995 hPa. This ensures that cyclones are sufficiently strong to be considered a TC.
- The TC genesis must be equator-ward of $\pm 35°$ latitude.
- TC cannot exist pole-ward of $\pm 60°$ latitude.
- The TC core must be warmer than the average 850 hPa temperature within the cyclone object. This ensures that the TC has a warm core. Optimally, temperatures at higher atmospheric levels should be used to assess the warm core structure of TCs (4–8 km height (Stern & Nolan, 2012)). Using the 850 hPa temperature is a compromise since we use this field for detecting frontal zones and want to minimize the number of necessary algorithm input variables.
- The minimum temperature with the TC at 850 hPa has to be $\geq$285 K.
- The mean cloud shield brightness temperature (Tb) over the TC object must be $\leq$241 K. This helps to eliminate cyclones that do not produce deep convection.

2.2.5 Atmospheric Fronts

We use the algorithm proposed by Parfitt et al. (2017) for detecting frontal zones. The frontal variable (F^*) is calculated as:

$$F^* = \zeta_p |\nabla(T_p)|, \tag{1}$$

where T is the air temperature at a pressure surface (p; here 850 hPa) and ζ_p is the curl of the wind vector that is normal to the pressure surface. Next, we calculate the non-dimensional and normalized frontal diagnostic F as:

$$F = \frac{F^*}{f|\nabla T|_0}, \tag{2}$$

where f is the Coriolis parameter at the corresponding latitude and $|\nabla T|_0 = 0.45\,\mathrm{K}/100\,\mathrm{km}$. Fronts are identified in grid cells where $F > 1$. An example of frontal zones is shown in brown contours Fig. 2d over Eastern Europe and south of France. A caveat in using this frontal definition is that grid cells close to the equator can not be analyzed since f becomes zero. Additionally, orographic effects on temperature and wind speed frequently introduce stationary fronts over mountain regions (e.g., see Fig. 2f), which complicates the analysis of fronts over areas with steep orographic gradients. We decided to only identify but not track frontal zones since the hourly input data from ERA5 is typically too coarse to connect thin and often fast-moving frontal zones in time.

2.2.6 Mesoscale Convective Systems (MCSs)

We identify mesoscale precipitation areas that include convective precipitation by using hourly GPM-IMERG precipitation on the ERA5 grid. In doing so, we mask all hourly precipitation grid cells with more than $2\,\mathrm{mm\,h^{-1}}$ and select contiguous areas that are $5{,}000\,\mathrm{km}^2$ for at least four hours. We call these features mesoscale precipitation objects.

Additionally, we track mesoscale ice cloud shields similarly to mesoscale precipitation objects. We mask all grid cells in the hourly regridded brightness temperature that have temperatures less than or equal to 241 K. We remove all features that do not have cloud shields $\geq 40{,}000\,^2$ for more than four hours. This or similar thresholds are widely used in identifying MCSs maddox1980mesoscale,feng2021

We define MCSs as a combination of a mesoscale precipitation object under a mesoscale ice cloud shield. However, we need additional criteria to make sure that the precipitation is originating from deep convection. Therefore, we demand a minimum cloud brightness temperature of $\leq$225 K at least once during the MCS lifetime (associated with overshooting cloud tops) and that the maximum hourly precipitation is more than $10\,\mathrm{mm\,h^{-1}}$ during the MCS lifetime. These criteria for MCS detection are similar to previous studies (A. Prein et al., 2021; Feng et al., 2021).

2.2.7 Atmospheric Rivers (ARs)

We use IVT to identify AR objects. ARs must have IVT values of at least $500\,\mathrm{kg\,m^{-1}\,s^{-1}}$ and last at least 9-hours. We decided to use a rather high $500\,\mathrm{kg\,m^{-1}\,s^{-1}}$ threshold since previous work has shown that it results in more reliable results when applied globally (Reid et al., 2020). All objects that fulfill this criterion are called IVT streams. To classify as an AR, IVT streams must be at least 2,000 km long and must be at least twice as long as wide (Neiman et al., 2008; Rutz et al., 2014; Reid et al., 2020; Guan & Waliser, 2015). Additionally, we demand that the centroid of an AR is poleward of $20\,^\circ$, which helps to eliminate persistent objects in the tropics that would otherwise classify as ARs.

3 Results

3.1 Case Studies of Interacting Phenomena During Extreme Precipitation Events

We illustrate MOAAP's multi-feature identification approach by showing the tracks and atmospheric conditions of three recent and extensively studied extreme precipitation events starting with the U.S. landfall of tropical cyclone Florence in September 2018 (Fig. 2a,b). The track of the TC is very similar to the track of its associated precipitation, cloud shield, and IVT stream objects (Fig. 2a). During landfall (Fig. 2b), Florence was fully wrapped within an IVT stream object meaning that it transported a large amount of moisture around its center. We can also detect frontal objects around the center of the TC indicating strong gradients in temperature and pressure. Importantly, an anticyclone object is detected northeast of Florence, which helped stall the system during landfall causing catastrophic flooding.

As a second example, we selected the northern Alpine flooding of August 2002 where a cutoff low developed over the Gulf of Genoa and slowly tracked northeastward producing large rainfall amounts (Fig. 2c,d). Cyclones with these tracks are known flood producers in this region and are called Vb-cyclones (Bebber, 1882; Hofstätter et al., 2018). The track of the cyclone, the cloud shield, the precipitation object, and the IVT stream develop in parallel at the beginning of the event and then start to deviate as the storm moves northeastward and weakens. The IVT stream object indicates the advection of moist air from the Mediterranean but in comparison to Florence, this storm is weaker and is not able to wrap the IVT object around its core. Anticyclones to the west, south, and east contributed to the slow movement speed of this cyclone.

The last example is an AR event that contributed to major flooding in California in January 2017. We can track the IVT stream and associated cloud shield from the middle of the North Pacific to landfall and beyond (Fig. 2e). The associated cyclone is fairly stationary and sometimes connects to a cyclone in the east resulting in a convoluted track. At landfall, the moisture flux towards the U.S. West Coast is amplified by a cyclone in the north and an anticyclone in the south. We will see later that this general pattern of an anticyclone, AR, cyclone (from south to north) is common during the landfall of heavily precipitating ARs.

3.2 Scale Analysis of Atmospheric Phenomena

Scale diagrams that visualize the time and spatial scale of various atmospheric phenomena, such as shown in Kotamarthi et al. (2016) (see their Fig. 7), are useful to understand the spatiotemporal characteristics of motions in the atmosphere. Such diagrams are typically based on expert knowledge. Fig. 3 shows a fully data-driven version of a scale diagram based on the tracking results in this study. We can sample meso-alpha to macro-alpha scales (Orlanski, 1975) and hours to weeks since ERA5 has a horizontal grid spacing of ∼30 km, hourly output, and we are tracking phenomena one month at a time, meaning that phenomena that life from one month to the next are split into two. While this increases the frequency of phenomena and reduces their duration, it has little effect on the overall statistics since most phenomena live much shorter than a month. We calculate the length scale of each phenomenon from its area by assuming circular shapes. MCSs are with an average lifetime of ∼10 hours and an average length of ∼200 km the smallest phenomena that we track while ARs are with 1,000 km and ∼2.7 days the largest and longest-lived. This is partly related to the criteria that ARs have to be at least 2,000 km long. Cyclones and anticyclones occupy a wide range of length scales with anticyclones typically being shorter-lived than cyclones. Large cyclones and anticyclones often occur in mid-latitudes while their polar counterparts are typically much smaller (not shown). TCs have similar average lifetimes as cyclones but have larger average length scales. There is a tendency that larger objects are also longer-lived. Generally, these results agree with expectations but the significant amount of overlap between the spatiotemporal space that different phenomena occupy is often misrepresented in existing scale diagrams.

3.3 Climatology of Atmospheric Phenomena

Fig. 4 shows the climatological frequency of phenomena and their month of peak occurrence. These frequencies represent the average number of days that a grid cell is occupied by a phenomenon. Note that this is not the track density but incorporates the phenomenon's spatial extent. Seasonal feature frequencies are shown in supplementary Fig. S1.

Cyclones feature a global hot spot of up to 200 days per year in the Southern Ocean around 60 °S and 120 °E (Fig. 4a). The northern hemisphere features the well known storm tracks in the North Pacific and North Atlantic. Cyclone frequencies typically peak in winter meaning during DJF in the northern hemisphere and JJA in the southern hemisphere (Fig. 4b). However, there are some noticeable exceptions such as an April peak of cyclones in the western and central U.S. or over northeast Asia. The spatial pattern of cyclone frequencies agrees well with previous studies (Neu et al., 2013; Ullrich & Zarzycki, 2017) but the absolute values are hard to compare since most studies present track densities instead of object frequencies. We believe showing the latter is more informative since it better represents the impact of a phenomenon on an area that can extend large distances from its center.

Anticyclones feature maxima north and south of the area of maximum cyclone frequency in both hemispheres (Fig. 4c). A band of high anticyclonic activity spans across the southern hemisphere at $\sim$40 °S, which persists through all seasons and migrates northward during JJA (Fig. 4d). There is also a high frequency of anticyclones over Antarctica. Over the northern hemisphere, anticyclone frequencies are highest in DJF and lowest in JJA with local maxima over the eastern parts of the Pacific and Atlantic basin, and the Beaufort Sea. Further hotspots exist over central Asia and Greenland that should be interpreted with caution since they are partly a result of interpolating surface pressure to sea level. These frequency patterns agree well with previously published data (Pepler et al., 2019).

AR frequencies show maxima over all mid-latitude ocean basins (Fig. 4e), and have a characteristic diagonal orientation (equator-ward in the west and pole-ward in the east) that is associated with hot spots in cyclones and anticyclones. ARs occur most frequently between these two hot spot regions and reach their peak frequency during JFM in most areas of the southern hemisphere while a clear seasonal progression is visible in the north-east Pacific and north-east Atlantic (Fig. 4f). Here, northern regions have a late summer peak changing to a winter peak in southern regions.

Our front detection algorithm frequently identifies stationary fronts over regions with steep topography (Fig. 4g). This is likely the reason why Parfitt et al. (2017), whose algorithm we apply, only showed results over ocean regions. Regions with the highest frontal activity are close to the east coasts in northern mid-latitudes. No prominent hotspots are visible over the southern hemisphere except for subtropical areas west of South America and Africa and coastal regions around Antarctica. Frontal statistics in the latter area are likely affected by strong land-ocean and orographic gradients. These general patterns agree well with results shown in Berry et al. (2011) and Parfitt et al. (2017) except for the hotspots in the subtropical southern Pacific and Atlantic. Fronts are most frequent during DJF over oceans in the northern hemisphere, while land regions frequently feature a spring peak (Fig. 4h). Over the southern hemisphere, fronts are most frequent during JJA.

MCSs are most common in the Intertropical Convergence Zone (ITCZ), particularly over the warm pool region, over the Amazon basin, and the Congo basin (Fig. 4i). In mid-latitudes, the La Plata basin and the Southeastern U.S. feature the highest activities. The different mechanisms that cause MCSs are visible in their seasonality (Fig. 4j). The northward and southward propagation of the ITCZ is visible in the tropical Atlantic and Pacific. Mid-latitude ocean regions feature winter-time maxima while mid-latitude land areas deviate from this pattern and show spring and summer peak frequencies.

TCs occur over sub-tropical and mid-latitude ocean regions with a global hotspot in the west Pacific (Fig. 4k). Our algorithm erroneously picks up TCs in the South Atlantic, which is similar to Ullrich et al. (2021) and might partly be related to using ERA5 data for TC identification. The seasonal peak months of TCs are late summer and early fall in both hemispheres (Fig. 4l).

3.4 Phenomena Contribution to Mean and Heavy Precipitation

In this subsection, we discuss the fractional contribution of each phenomenon's precipitation to total annual precipitation and how frequently each phenomenon contributes to the top 99th percentile hourly precipitation events at each grid cell (Fig. 5). We incorporate the precipitation within each object's extent and the precipitation under mesoscale ice cloud shields that are intersecting with the phenomenon. E.g., for TCs we account for the precipitation in the area of the low-pressure anomaly and the precipitation in the adjacent ice cloud shield.

Commonly we do not associate anticyclones with precipitation and this is true for their core regions but precipitation frequently originates across their pole-ward flanks such as shown for the land-falling AR in Fig. 2f. This most often happens in the South Atlantic where some regions experience more than 40 % of their annual rainfalls in the vicinity of anticyclones (Fig. 5a). In the northern hemisphere, the Karakoram region is the hot spot for precipitation under anticyclonic influence, which is related to the frequently detected anticyclones over steep topography partly originating from extrapolating surface pressure from high altitudes to mean sea level. Concerning extreme precipitation, anticyclones can play an important role in mid-latitude ocean basins, particularly in the South Atlantic and parts of the South Indian Ocean (Fig. 5b).

Cyclonic rainfall contributions are shifted poleward from those of anticyclones (Fig. 5c). The Northeast Atlantic is the global hotspot for cyclonic precipitation with more than 50 % of the annual rainfall related to cyclonic activity. Other regions with more than 40 % cyclonic precipitation are in the Northeast and Northwest Pacific, the South Atlantic, and the Southern Indian Ocean. All ocean regions pole-ward of $\pm 30°$, except for the southeast Pacific, receive more than 50 % (with peaks of more than 90 %) of their hourly heavy precipitation from cyclones. The West Coast and eastern part of North America, parts of Europe, Japan, and parts of central Asia are land hotspots for heavy cyclonic precipitation (Fig. 5c).

TCs are a very small subset of cyclones that contribute little to total precipitation except for a small area in the West Pacific that gets more than 20 % of its annual rainfall from TCs (Fig. 5e). The values presented here are smaller than in previous studies – e.g., by Rodgers et al. (2001) or Jiang and Zipser (2010), compare to their Fig. 5d). This has two reasons. First, we systematically under-count TC frequencies in areas that Jiang and Zipser (2010) identified as hot spots such as the Northeast and Northwest Pacific, and second, rather than using a fixed radius around the center of a TC (typically $\sim$500 km is used), we account for precipitation in the TC object (low-pressure anomaly, see Fig.2b) and precipitation underneath the TC cloud shield. The latter will result in not accounting for TC precipitation in remote cloud bands that are not directly connected to the system. TC contributions to extreme hourly rainfall can reach up to 50 % in the Northwest Pacific but are low otherwise (Fig. 5f). This low contribution of TCs to extreme hourly rainfall might be surprising but it is predominantly due to their rarity and their relative contribution to extremes is higher when investigating rarer (more intense) extreme precipitation events as we will show later.

Precipitation from AR accounts for more than 50 % of annual precipitation over the central regions of mid-latitude ocean basins. There is little AR rainfall contribution over land except for islands and coastal areas (Fig. 5e). The magnitude and location where ARs contribute to heavy rainfall are similar to those of CY (except over land), which is not surprising since those two phenomena are closely linked (e.g., see Fig. 2c). Our results agree well with previous analyses and highlight similar hot spot regions of extreme precipitation contributions from ARs (Waliser & Guan, 2017).

MCSs contribute the majority of precipitation in the tropics and some mid-latitude land regions such as Southeast South America and the Central U.S., which is in good agreement with published literature (Nesbitt et al., 2006; Feng et al., 2021) (Fig. 5g). Even higher contributions of MCSs are found for extreme hourly precipitation with rates of more than 80 % in the tropics, subtropics, the eastern U.S., large parts of Sub-Saharan Africa, South America, and China (Fig. 5h).

3.5 Phenomena Related to Extreme Precipitation Events

Here we investigate what phenomena were present in a 1,000 km radius around the top 100 heaviest hourly precipitation events in each IPCC AR6 region (Iturbide et al., 2020). Note that this method results in selecting much rarer events compared to using the 99th percentile of hourly rainfall in each grid cell used in the previous section.

Fig. 7 shows that interactions between phenomena during extreme hourly precipitation events are the norm and not the exception in most regions. For instance, the Eastern North America (ENA) region gets all of its top 100 hourly extreme rainfall events from MCSs, 70 % of them are near a front, ∼50 % are in the vicinity of a cyclone, ∼40 % are near an anticyclone or AR, and 10 events are related to a TC. Most tropical regions get the majority of their extreme hourly precipitation events from MCSs while cyclones become dominant in higher latitudes. ARs are major contributors to hourly extreme precipitation events on the west coast of North America (WNA and NWN region; Waliser and Guan (2017)) northern Europe (NEU; Lavers and Villarini (2013)), southern South America (SSA; Viale et al. (2018)), New Zealand (NZ; Reid et al. (2021)), and the south Atlantic Ocean. Surprising is the frequent presence of anticyclones in the vicinity of extreme precipitation in mid and high latitudes.

We find similar results when considering the top 100 daily extreme precipitation events (see supplementary Fig. S2). Noteworthy differences include the higher contribution of TCs to daily compared to hourly events in regions around the northwest and the southwest Pacific Ocean, and the much larger contribution from CY in central and eastern North America, and Southeast South America. These differences are likely caused by the increasing importance of rainfall duration for daily extreme events compared to hourly extremes. TCs and CY have much longer lifetimes than MCSs (see Fig. 3) and can therefore create longer duration rainfall and higher daily accumulations when storm motion slows.

The contribution of atmospheric phenomenon to extreme precipitation is a function of the rarity of extreme events. Fig. 8 shows the relative contribution of each phenomena to extreme hourly precipitation as a function of event intensity (e.g., the 10th event includes the top 10 most intense precipitation events). For instance, in South Eastern South America (SES) MCSs in combination with fronts and anticyclones were present in the most intense precipitation events while weaker events are more frequently influenced by CY and ARs. In Northern Australia (NAU), East Asia (EAS), and eastern North America (ENA) TCs are gaining in importance with increasing event rarity. Supplementary Fig. S3 shows the same statistics for daily precipitation extremes. While differences depend on the region, there is a tendency of stronger cyclonic influence during the rarest daily extreme events compared to hourly events in many regions.

To better understand which phenomena combinations are interacting during extreme precipitation events we show the frequency of phenomena co-occurrences in Fig. 9. The fewest interactions are found in tropical ocean regions where stand-alone MCSs are the most common source of extreme events. However, MCSs combined with frontal zones are also common. Mid-latitude regions show more complex interactions. For instance, west-central Europe (WCE) features frequent interactions between anticyclones, CY, and fronts. AR-related extreme precipitation events are frequently co-occurring with a pair of CY and anticyclones as visible in the example in Fig. 2. Generally, the combined occurrence of CY and anticyclones is a common feature in many mid-latitude regions during extreme events. Results for daily extreme events are similar (Supplementary Fig. S4) with the most noticeable differences in mid-latitudes where interactions with cyclones increase in importance, and in northern high-latitudes where phenomena interactions decrease in general.

4 Summary and Discussion

In this study, we present the Multi Object Analysis of Atmospheric Phenomenon (MOAAP) algorithm to identify extratropical and tropical cyclones, anticyclones, ARs, MCSs, and frontal zones and applied it to historical data to better understand how these features are related to mean and extreme precipitation on a global scale. The main advantage of using a multi-feature-based approach compared to single-feature-based methods that are most common in the existing literature is that it allows us to study interactions between phenomena in extreme precipitation-producing environments. Such interactions are known to be important (Barlow et al., 2019) but are understudied systematically on a global scale.

Many approaches exist in the published literature to identify and track individual phenomena such as TC, cyclones, or ARs. Where available, we established methods to maximize the quality of the phenomenon classification. We alsominimized the amount of input data, and used variables that are standard model outputs. The main results and conclusions from this study are:

- Extreme hourly and daily precipitation events are typically caused by multiple atmospheric phenomena that interact on different scales and maximize local precipitation rates. This is intuitive since the need for the alignment and interaction of multiple phenomena is the prime reason why those events are rare and agrees with previous studies over North America (Barlow et al., 2019). Therefore, associating extreme precipitation events to a single atmospheric process can be misleading and often oversimplifies the multi-scale interactions involved. It is also important to note that the investigated phenomena are not physically or statistically independent of each other (e.g., cyclones typically have frontal systems).
- MCSs dominate the water cycle in the tropics and continental areas of the subtropics such as the Eastern U.S., Southeast South America, and parts of Southern Africa in agreement with previous findings (Nesbitt et al., 2006; Feng et al., 2021). Hourly and daily precipitation extremes are almost exclusively related to MCSs in these regions.
- TCs are a minor contributor to the global water cycle and are of secondary importance for extreme hourly and daily precipitation production. However, this is mainly due to how we define extremes in our analyses and TCs might play a much more significant role in extreme statistics when higher-end extremes would be considered (e.g., the one-in-a-hundred-year event). The advent of such high-resolution climate modeling (Haarsma et al., 2016) and particularly km-scale climate modeling (A. F. Prein et al., 2015; Stevens et al., 2019; Mahoney et al., 2021) could help to alleviate some of the observational record-length issues that limit our understanding of high-impact extreme events.
- At higher latitudes, pairs of cyclones and anticyclones play an important role in extreme precipitation production. The co-occurrence of these two phenomena increases moisture convergence and transport. This is a prime mechanism in regions with strong AR events but also plays an important role in other regions such as in central and Northeastern Asia.

The findings listed above should be interpreted alongside the following caveats related to our approach.

- The frontal detection algorithm often identifies fronts over steep topography and coastlines. This leads to an overestimation of precipitation related to fronts in these regions. Additionally, hourly model output is typically not sufficient to track frontal objects and only allowes us to study them as 2D features.
- The TC tracking algorithm could be improved, particularly in the South Atlantic and South Pacific basins. Identifying warm cores at higher tropospheric levels would be beneficial but would increase the input data volume.
- The thresholds to identify phenomena (see Table 1) could be scale dependent and might have to be re-tuned particularly when applied to much coarser resolution data (i.e., one degree or larger). The thresholds can be easily changed in the MOAAP algorithm to optimize it to various input datasets.
- IMERG precipitation does not cover high latitudes and smooths out hourly precipitation features (Guilloteau & Foufoula-Georgiou, 2020). Additionally, deficiencies have been reported over mountain regions (Bartsotas et al., 2018; G. Huffman, 2019). The results presented here should, therefore, be interpreted with caution over high-mountain and high-latitude regions.

Future work will focus on addressing these caveats. Additionally, MOAAP will be applied as a lagrangian evaluation tool to global and regional climate model simulations and to improve our understanding of climate change impacts on the occurrence of phenomena, phenomena characteristics, and their relation to mean and extreme precipitation. Adding additional phenomena such as jet streams or smaller scale convection and phenomena in the land surface or ocean could provide further insights into the physical processes contributing to extreme precipitation, particularly in phenomena interactions in the coupled earth system. Finally, the results from this feature-based analysis could be used to train machine learning algorithms, most of which currently rely on labeling features by hand (Kashinath et al., 2021).

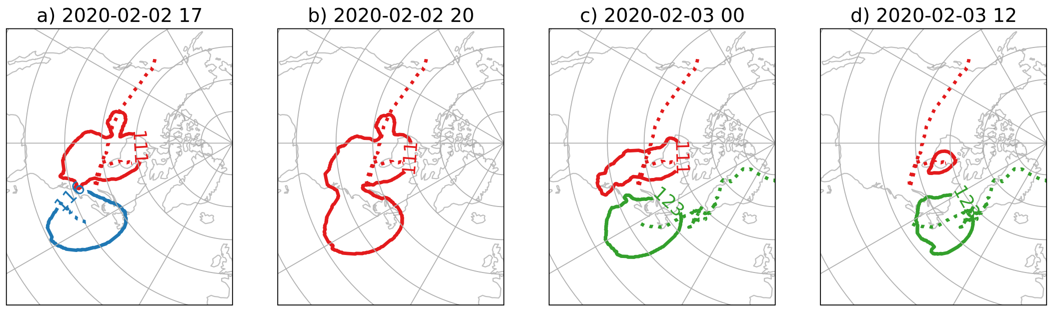

Figure 1. Example for merging and tracking of cyclones over eastern North America. Cyclone number 111 (red) and 110 (blue) collide on Feb. 2, 2020 (a) resulting in the termination of the smaller cyclone (110, b). Six hours later, cyclone 111 splits into two cyclones resulting in the genesis of a new cyclone (123, c). Dotted lines show the track of each cyclone. Cyclone 111 ends over Hudson Bay and cyclone 123 moves over Greenland and enters the Arctic Ocean (d).

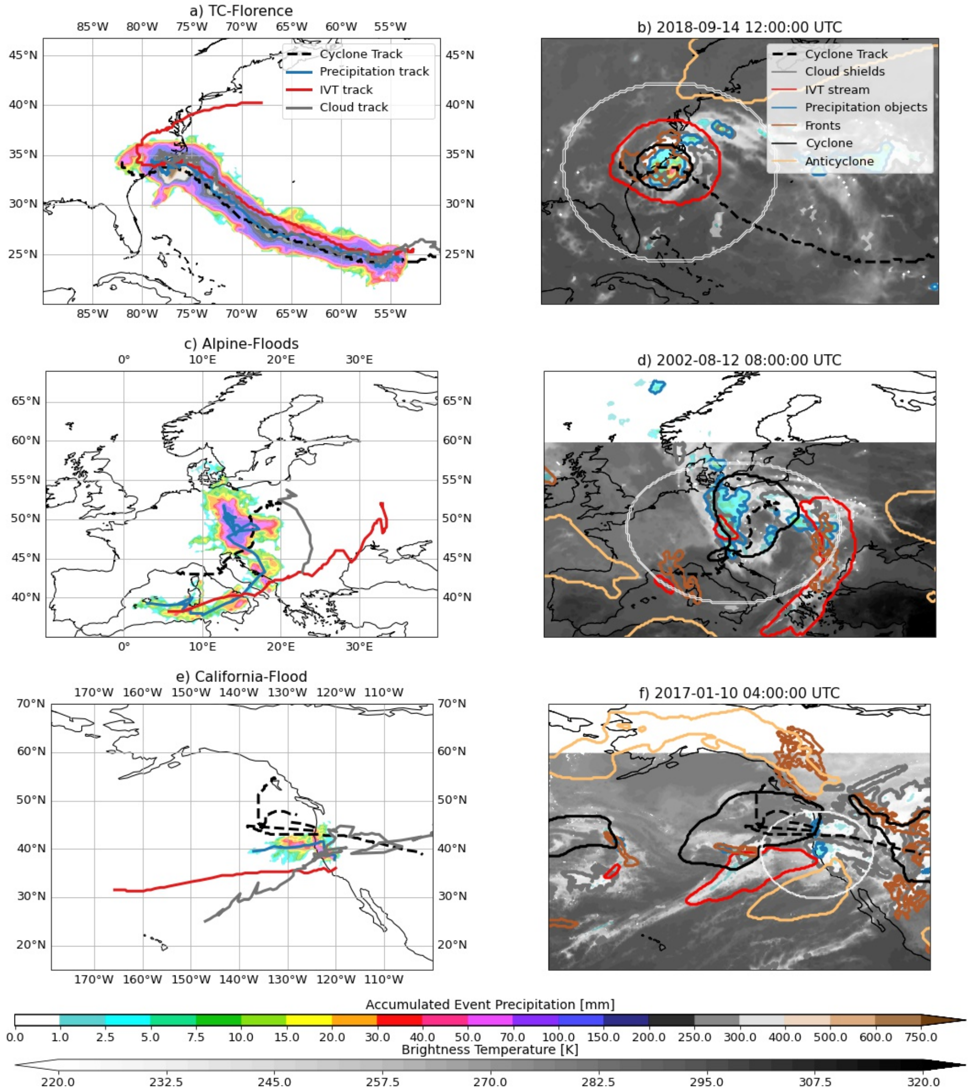

Figure 2. Involved features during the extreme precipitation related to tropical cyclone (TC) Florence in 2018 (a,b), the 2003 Northern Alpine floods (c,d), and the AR event that contributed to the floods in California in early 2017. Colored-filled contours in the left panels show accumulated precipitation from the precipitation feature that resulted in severe flooding. Additionally, the track of involved cyclones (dashed black line), IVT streams (red line), cold cloud tops (grey lines), and the precipitation object (blue line) are shown. The right panels show a snap-shot of the synoptic situation during the flood events with satellite brightness temperature (gray contours), the cyclone track (dashed black line), the outline of the cyclone object (black contour), the IVT object (red contour), cold cloud objects (gray contour), anticyclones (light brown contours), and frontal zones (dark brown). The white circle indicated the 1,000 km search radius that is used to associate phenomena to extreme rainfall events.

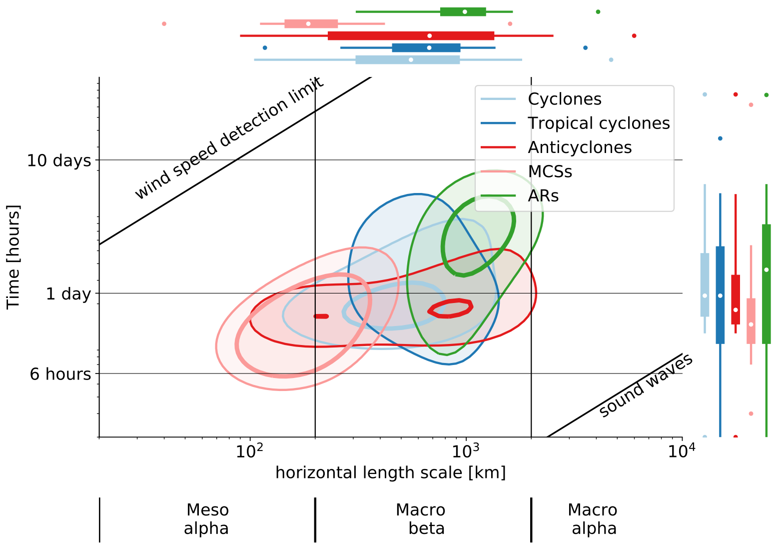

Figure 3. Characteristic feature horizontal length scale (x-axis) and time scale (y-axis) for cyclones (light blue), tropical cyclones (dark clue), MCSs (light red), anticyclones (dark red), and ARs (green). The contours show 2-dimensional Gaussian kernel density estimates with a bandwidth of 0.4 that was applied to the logarithm of the data. The box-whisker plots show the median (white dot), interquartile range (boxes), 5th to 95th percentile (whiskers), and maximum and minimum (colored circles).

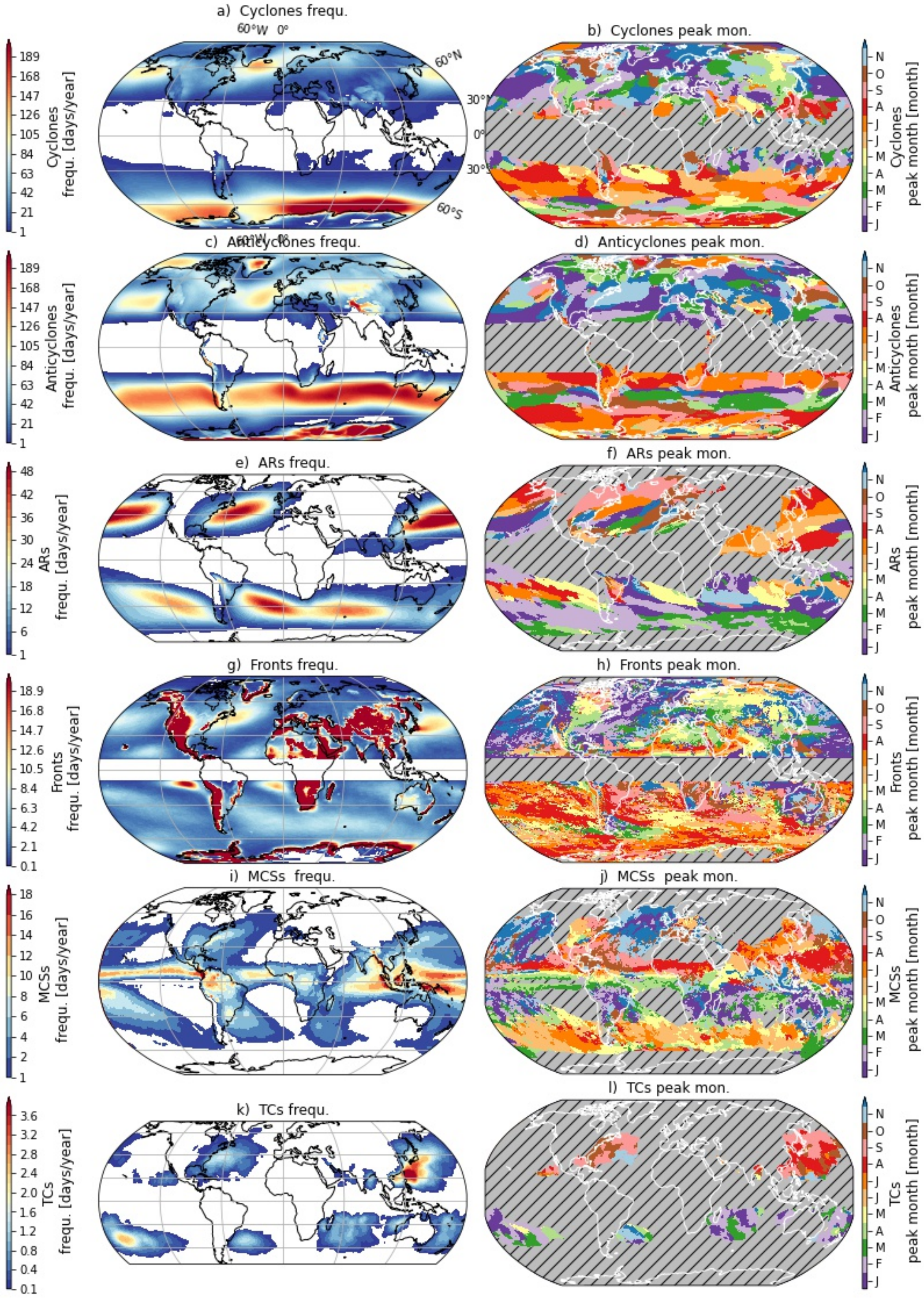

Figure 4. Annual frequency of cyclones, anticyclones, ARs, fronts, MCSs, and TCs features are shown top-down in the left column. The right column shows the color-coded month with their maximum frequency.

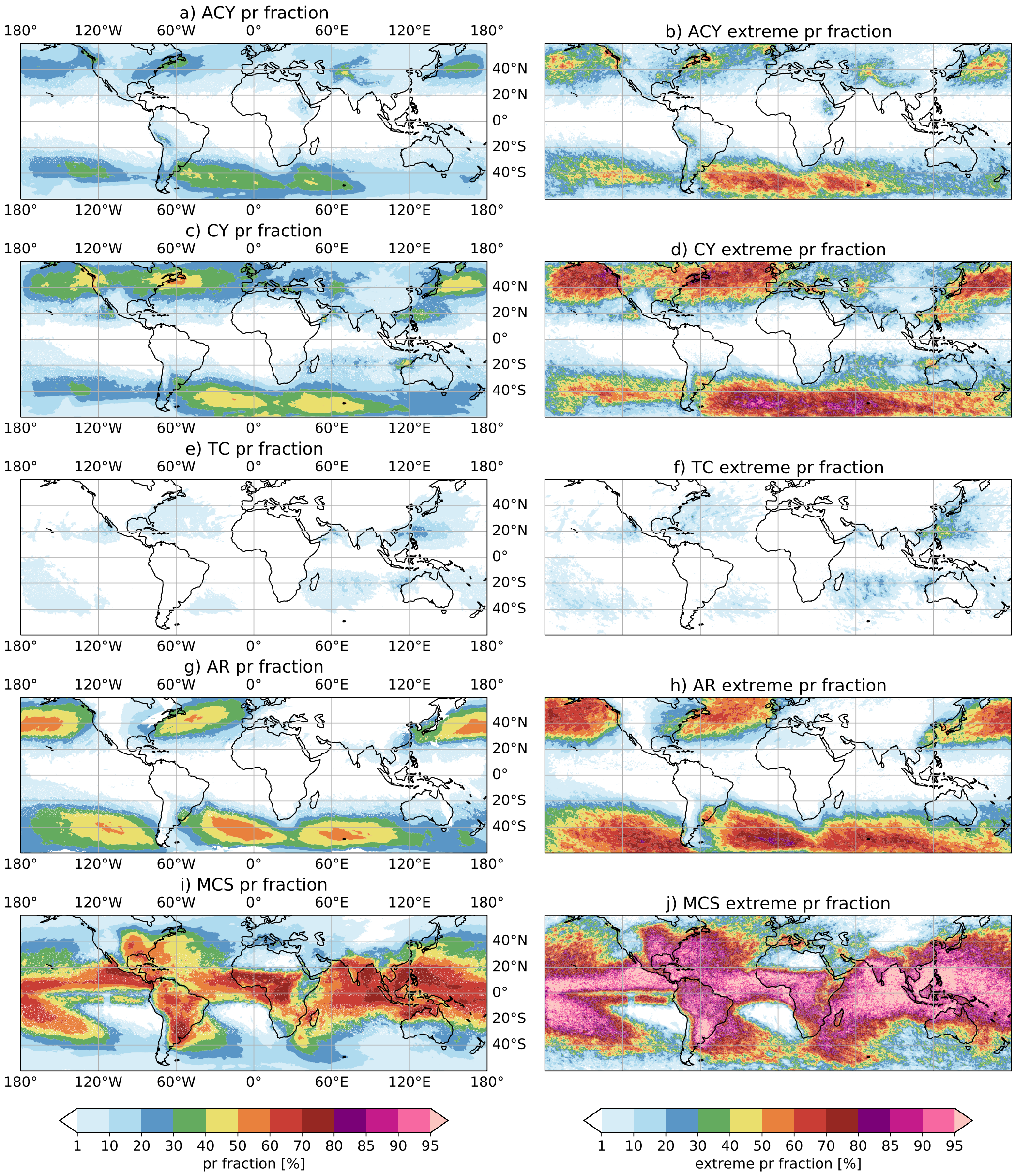

Figure 5. Fraction of precipitation from anticyclones, cyclones, TCs, ARs, and MCSs (top-down) to total precipitation (left column) and the fraction of 99th percentile hourly precipitation event occurrence from each phenomenon (right column).

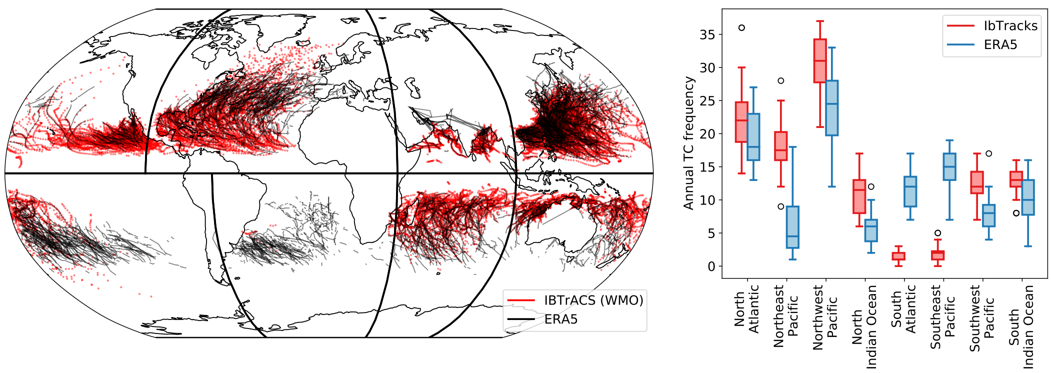

Figure 6. Tropical cyclone tracks from the IBTrACS WMO (red) and our results from tracking TCs in ERA5 (black) over the period 2001–2020 (left). Only category 1 or stronger tropical cyclones on the Saffir-Simpson scale are shown. Annual frequency of TCs in each major ocean basis (right). Box-whisker statistics show the inter-annual variability.

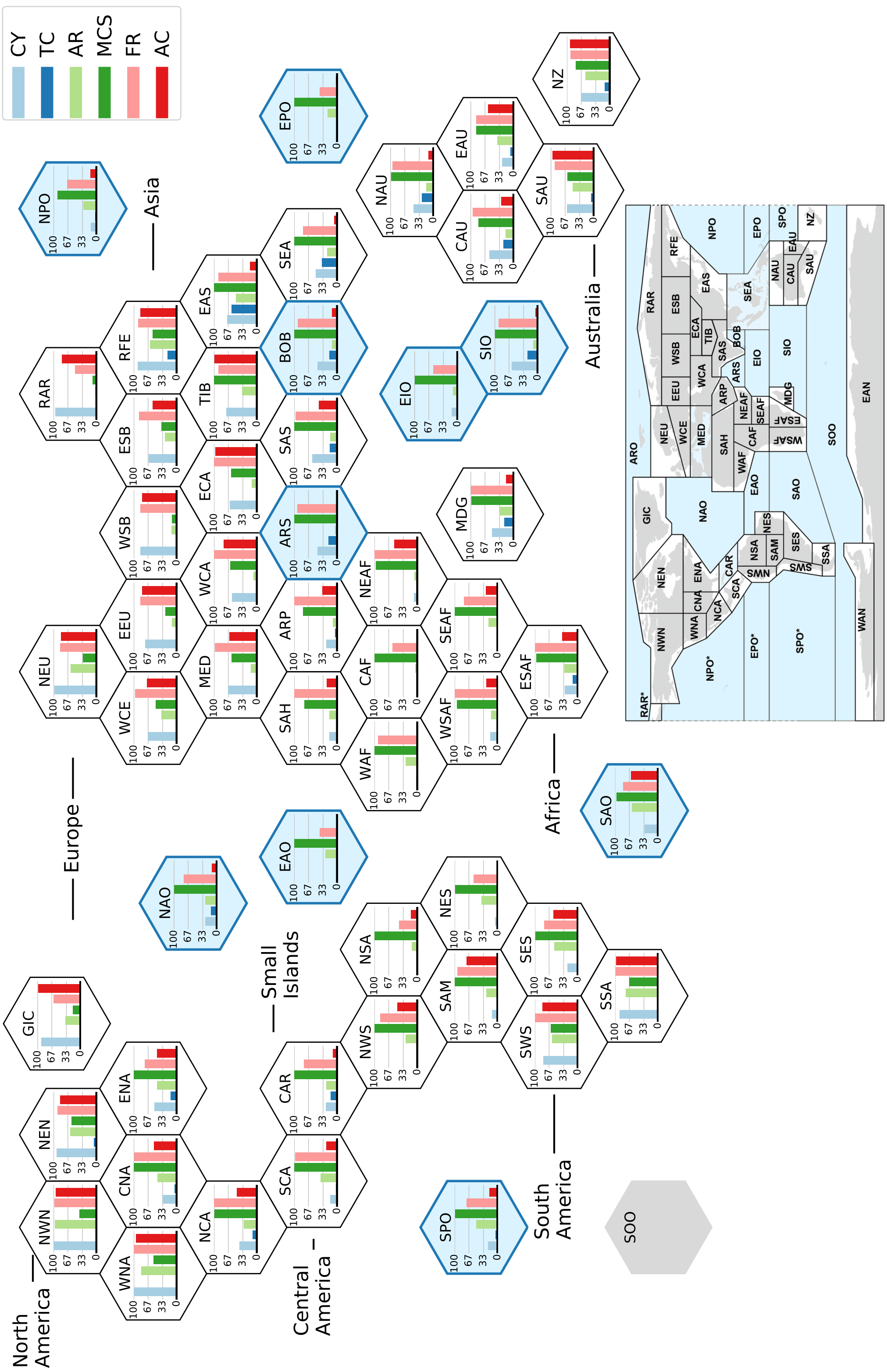

Figure 7. Frequency of features in the vicinity (1,000 km radius) of extreme precipitation events in IPCC AR6 regions. We consider the 100 most extreme hourly precipitation events in each region based on GPM-IMERG precipitation. Blue hexagons indicate ocean regions and grey hexagons do not contain GPM-IMERG precipitation data. The location of each region is shown in the map-inlet in the lower right corner (taken from Iturbide et al. (2020)).

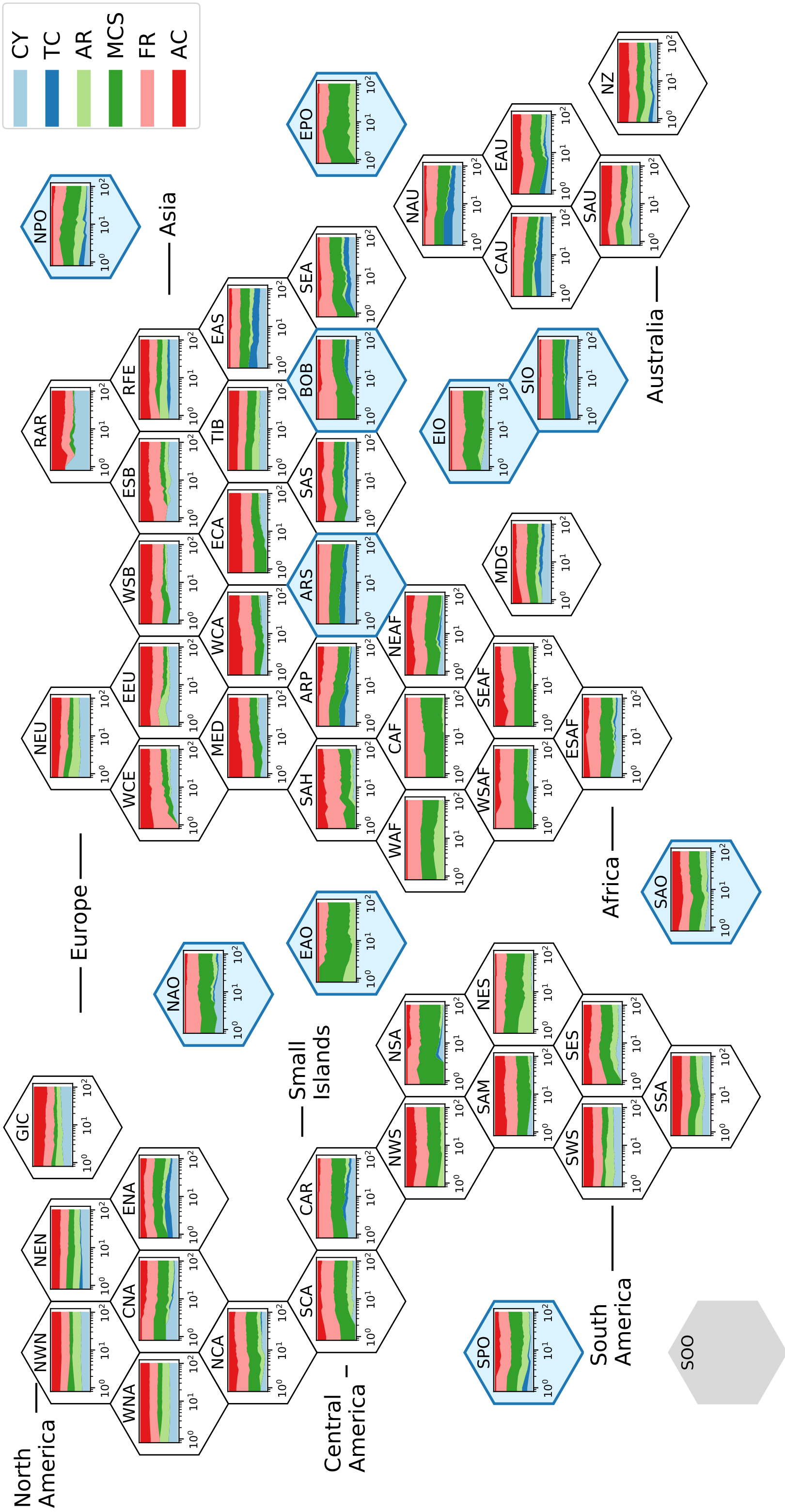

Figure 8. As Fig. 7 but showing the percent contribution (vertical axis) of atmospheric features dependent on the intensity of the extreme precipitation events with the rarest event on the left and all of the 100 most extreme precipitation events on the right.

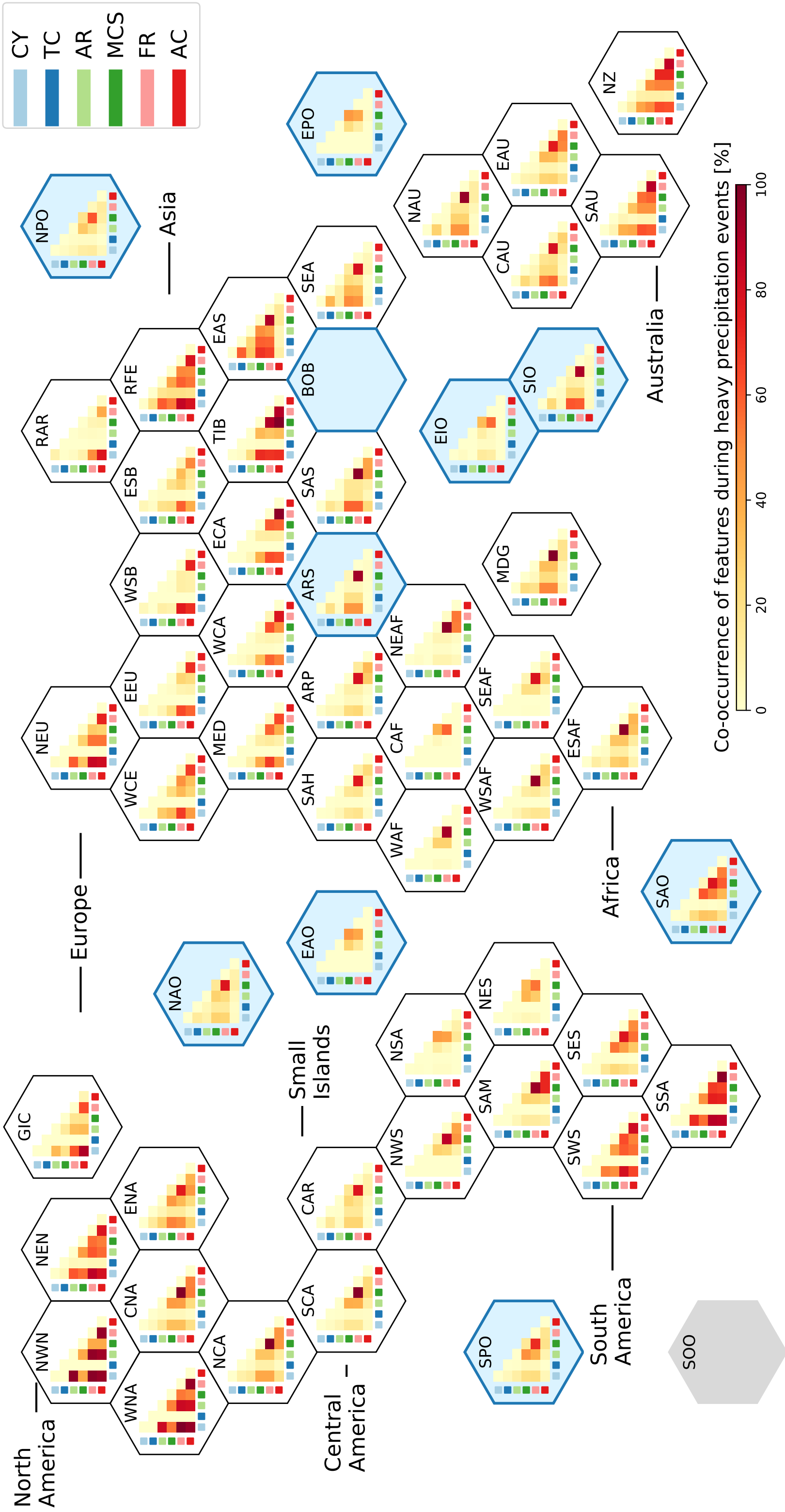

Figure 9. Showing the same data as in Fig. 7 but highlighting the co-occurrence of features during extreme precipitation events. The colors in the heatmaps show the percent of the time at which features co-occurred. The colors beneath the x- and y-axis show the feature as indicated in the legend.

Table 1. Criteria used for feature classification. The following acronyms are used in the table: pressure (P), moisture stream (MS), integrated vapor transport (IVT), brightness temperature (Tb), temperature (T), area (A), the standard deviation of Gaussian smoother (σ; values in brackets correspond to the time, latitude, and longitude dimension).

Feature	Intensity Thresholds	Temporal	Spatial/Area	Additional Criteria	Breakup
Cyclones	$P_{anom} \leq$ -8 hPa	12-hours			yes
Anticyclones	$P_{anom} \geq 6$ hPa	12-hours			yes
IVT Streams	$MS_{min} \geq 0.13$ g/g×m/s	9-hours	$A_{IVT} \geq 100{,}000\,km^2$		yes
ARs	IVT ≥ 500 kg/ms	9-hours		min. length $\geq 2{,}000$ km; length/width ≥ 2; lat. centroid $\geq \pm 20°$	yes
Mesoscale Cloud Shields	Tb ≤ 241 K	9-hours	σ=[0,1,1]; $A_{CL} \geq 40{,}000\,km^2$		no
Mesoscale Precipitation Areas	PR ≥ 2 mm/h	3-hours	σ=[0,1,1]; A_{PR}=5,000 km2		no
Mesoscale Convective Systems	max. PR≥ 3 mm/h; Tb ≤ 241 K; min Tb ≤ 225 K	3-hours	$A_{PR \geq 2mm/h} \geq 2{,}500\,km^2$; $A_{Tb \geq 241\,K} \geq 40{,}000\,km^2$	Must be a mesoscale precipitation area and under a mesoscale cloud shield	no
Tropical Cyclones	$P_{min} \leq 995$ hPa; Tb ≤ 241 K; warm core T850 $\geq 0\,°C$; mean $T_{850hPa} \geq 285$ K			max. lat genesis $\leq \pm 35°$; max. lat $\leq \pm 65°$	no
Fronts			$A_{FR} \geq 50{,}000\,km^2$	lat. $\geq \pm 10°$	no

Acknowledgments

The FRONTIER project has received funding from the Research Council of Norway (project number 301777). NCAR is partly sponsored by the National Science Foundation under the Cooperative Agreement No. 1852977. We would like to acknowledge high-performance computing support from Cheyenne (doi:10.5065/D6RX99HX) provided by NCAR's Computational and Information Systems Laboratory, sponsored by the National Science Foundation.

Open Research

ERA-5 reanalysis data can be accessed from the Copernicus Climate Data Store (Copernicus, 2023). The GPM_MERGIR brightness temperature observations can be downloaded from the NASA server (GPM-MERGIR, 2023) and GPM-IMERG precipitation data can also be accessed from NASA (GPM-IMERG, 2023). The MOAAP code can be downloaded from GitHub (Prein, Andreas F, 2023).

References

Bardin, M. Y., & Polonsky, A. (2005). North Atlantic oscillation and synoptic variability in the European-Atlantic region in winter. *Izvestiya atmospheric and oceanic physics*, *41*(2), 127–136.

Barlow, M., Gutowski, W. J., Gyakum, J. R., Katz, R. W., Lim, Y.-K., Schumacher, R. S., … others (2019). North American extreme precipitation events and related large-scale meteorological patterns: a review of statistical methods, dynamics, modeling, and trends. *Climate Dynamics*, *53*(11), 6835–6875.

Bartsotas, N., Anagnostou, E., Nikolopoulos, E., & Kallos, G. (2018). Investigating satellite precipitation uncertainty over complex terrain. *Journal of Geophysical Research: Atmospheres*, *123*(10), 5346–5359.

Bebber, J. v. (1882). *Typische Witterungserscheinungen* (Tech. Rep.). arch. d. Deutschen Seewarte.

Berry, G., Reeder, M. J., & Jakob, C. (2011). A global climatology of atmospheric fronts. *Geophysical Research Letters*, *38*(4).

Blender, R., & Schubert, M. (2000). Cyclone tracking in different spatial and temporal resolutions. *Monthly Weather Review*, *128*(2), 377–384.

Clark, A. J., Bullock, R. G., Jensen, T. L., Xue, M., & Kong, F. (2014). Application of object-based time-domain diagnostics for tracking precipitation systems in convection-allowing models. *Weather and Forecasting*, *29*(3), 517–542.

Copernicus. (2023). *ERA5 hourly data on single levels from 1979 to present [Dataset].* Retrieved from `https://climate.copernicus.eu/climate-reanalysis` doi: 10.24381/cds.adbb2d47

Davis, C. A., Brown, B. G., Bullock, R., & Halley-Gotway, J. (2009). The method for object-based diagnostic evaluation (MODE) applied to numerical forecasts from the 2005 NSSL/SPC Spring Program. *Weather and Forecasting*, *24*(5), 1252–1267.

Feng, Z., Leung, L. R., Liu, N., Wang, J., Houze Jr, R. A., Li, J., … Guo, J. (2021). A global high-resolution mesoscale convective system database using satellite-derived cloud tops, surface precipitation, and tracking. *Journal of Geophysical Research: Atmospheres*, *126*(8), e2020JD034202.

GPM-IMERG. (2023). *GPM-IMERG half-hourly precipitation retrieval [Dataset].* Retrieved from `https://gpm.nasa.gov/data/imerg`

GPM-MERGIR. (2023). *GPM-IMERG half-hourly brightness temperature observations [Dataset].* Retrieved from `https://disc.gsfc.nasa.gov/datasets/GPM_MERGIR_1/summary`

Guan, B., & Waliser, D. E. (2015). Detection of atmospheric rivers: Evaluation and application of an algorithm for global studies. *Journal of Geophysical Research:*

Atmospheres, *120*(24), 12514–12535.
Guilloteau, C., & Foufoula-Georgiou, E. (2020). Multiscale evaluation of satellite precipitation products: Effective resolution of IMERG. In *Satellite precipitation measurement* (pp. 533–558). Springer.
Haarsma, R. J., Roberts, M. J., Vidale, P. L., Senior, C. A., Bellucci, A., Bao, Q., ... others (2016). High resolution model intercomparison project (HighResMIP v1. 0) for CMIP6. *Geoscientific Model Development*, *9*(11), 4185–4208.
Hersbach, H., Bell, B., Berrisford, P., Hirahara, S., Horányi, A., Muñoz-Sabater, J., ... others (2020). The era5 global reanalysis. *Quarterly Journal of the Royal Meteorological Society*, *146*(730), 1999–2049.
Hodges, K., Cobb, A., & Vidale, P. L. (2017). How well are tropical cyclones represented in reanalysis datasets? *Journal of Climate*, *30*(14), 5243–5264.
Hodges, K. I., Hoskins, B. J., Boyle, J., & Thorncroft, C. (2003). A comparison of recent reanalysis datasets using objective feature tracking: Storm tracks and tropical easterly waves. *Monthly Weather Review*, *131*(9), 2012–2037.
Hofstätter, M., Lexer, A., Homann, M., & Blöschl, G. (2018). Large-scale heavy precipitation over central Europe and the role of atmospheric cyclone track types. *International Journal of Climatology*, *38*, e497–e517.
Huffman, G. (2019). *IMERG V06 quality index.* Retrieved from `https://gpm.nasa.gov/sites/default/files/2020-02/IMERGV06_QI_0.pdf`
Huffman, G. J., Bolvin, D. T., Braithwaite, D., Hsu, K., Joyce, R., Xie, P., & Yoo, S.-H. (2015). NASA global precipitation measurement (GPM) integrated multi-satellite retrievals for GPM (IMERG). *Algorithm Theoretical Basis Document (ATBD) Version*, *4*, 26.
Huffman, G. J., Bolvin, D. T., Nelkin, E. J., & Tan, J. (2015). Integrated Multi-satellitE Retrievals for GPM (IMERG) technical documentation. *Nasa/Gsfc Code*, *612*(47), 2019.
Iturbide, M., Gutiérrez, J. M., Alves, L. M., Bedia, J., Cerezo-Mota, R., Cimadevilla, E., ... others (2020). An update of IPCC climate reference regions for subcontinental analysis of climate model data: definition and aggregated datasets. *Earth System Science Data*, *12*(4), 2959–2970.
Janowiak, J., Joyce, B., & Xie, P. (2017). *Merged IR V1, Edited by Andrey Savtchenko, Greenbelt, MD, Goddard Earth Sciences Data and Information Services Center (GES DISC).* `https://disc.gsfc.nasa.gov/datasets/GPM_MERGIR_1/summary`. (Accessed: 2022-03-15) doi: 10.5067/P4HZB9N27EKU
Jiang, H., & Zipser, E. J. (2010). Contribution of tropical cyclones to the global precipitation from eight seasons of TRMM data: Regional, seasonal, and interannual variations. *Journal of climate*, *23*(6), 1526–1543.
Kashinath, K., Mudigonda, M., Kim, S., Kapp-Schwoerer, L., Graubner, A., Karaismailoglu, E., ... others (2021). ClimateNet: an expert-labeled open dataset and deep learning architecture for enabling high-precision analyses of extreme weather. *Geoscientific Model Development*, *14*(1), 107–124.
Knapp, K. R., Kruk, M. C., Levinson, D. H., Diamond, H. J., & Neumann, C. J. (2010). The international best track archive for climate stewardship (IBTrACS) unifying tropical cyclone data. *Bulletin of the American Meteorological Society*, *91*(3), 363–376.
Kotamarthi, R., Mearns, L., Hayhoe, K., Castro, C. L., & Wuebbles, D. (2016). *Use of climate information for decision-making and impacts research: State of our understanding* (Tech. Rep.). Argonne National Laboratory Argonne United States.
Kunkel, K. E., Easterling, D. R., Kristovich, D. A., Gleason, B., Stoecker, L., & Smith, R. (2012). Meteorological causes of the secular variations in observed extreme precipitation events for the conterminous United States. *Journal of Hydrometeorology*, *13*(3), 1131–1141.

Lavers, D. A., & Villarini, G. (2013). The nexus between atmospheric rivers and extreme precipitation across Europe. *Geophysical Research Letters*, *40*(12), 3259–3264.

Lin, Y., & Mitchell, K. E. (2005). 1.2 the NCEP stage II/IV hourly precipitation analyses: Development and applications. In *Proceedings of the 19th conference hydrology, american meteorological society, san diego, ca, usa* (Vol. 10).

Mahoney, K., McColl, C., Hultstrand, D. M., Kappel, W. D., McCormick, B., & Compo, G. P. (2021). Blasts from the past: Reimagining historical storms with model simulations to modernize dam safety and flood risk assessment. *Bulletin of the American Meteorological Society*, 1–35.

Messmer, M., Gómez-Navarro, J. J., & Raible, C. C. (2015). Climatology of Vb cyclones, physical mechanisms and their impact on extreme precipitation over Central Europe. *Earth system dynamics*, *6*(2), 541–553.

Neiman, P. J., Ralph, F. M., Wick, G. A., Lundquist, J. D., & Dettinger, M. D. (2008). Meteorological characteristics and overland precipitation impacts of atmospheric rivers affecting the West Coast of North America based on eight years of SSM/I satellite observations. *Journal of Hydrometeorology*, *9*(1), 22–47.

Nesbitt, S. W., Cifelli, R., & Rutledge, S. A. (2006). Storm morphology and rainfall characteristics of TRMM precipitation features. *Monthly Weather Review*, *134*(10), 2702–2721.

Neu, U., Akperov, M. G., Bellenbaum, N., Benestad, R., Blender, R., Caballero, R., ... others (2013). IMILAST: A community effort to intercompare extratropical cyclone detection and tracking algorithms. *Bulletin of the American Meteorological Society*, *94*(4), 529–547.

Orlanski, I. (1975). A rational subdivision of scales for atmospheric processes. *Bulletin of the American Meteorological Society*, 527–530.

Parfitt, R., Czaja, A., & Seo, H. (2017). A simple diagnostic for the detection of atmospheric fronts. *Geophysical Research Letters*, *44*(9), 4351–4358.

Pepler, A., Dowdy, A., & Hope, P. (2019). A global climatology of surface anticyclones, their variability, associated drivers and long-term trends. *Climate Dynamics*, *52*(9), 5397–5412.

Poujol, B., Prein, A. F., & Newman, A. J. (2020). Kilometer-scale modeling projects a tripling of Alaskan convective storms in future climate. *Climate Dynamics*, *55*(11), 3543–3564.

Prein, A., Rasmussen, R., Wang, D., & Giangrande, S. (2021). Sensitivity of organized convective storms to model grid spacing in current and future climates. *Philosophical Transactions of the Royal Society A*, *379*(2195), 20190546.

Prein, A. F., Langhans, W., Fosser, G., Ferrone, A., Ban, N., Goergen, K., ... others (2015). A review on regional convection-permitting climate modeling: Demonstrations, prospects, and challenges. *Reviews of geophysics*, *53*(2), 323–361.

Prein, A. F., Liu, C., Ikeda, K., Bullock, R., Rasmussen, R. M., Holland, G. J., & Clark, M. (2020). Simulating North American mesoscale convective systems with a convection-permitting climate model. *Climate Dynamics*, *55*(1), 95–110.

Prein, Andreas F. (2023). *Multi Object Analysis of Atmospheric Phenomenon (MOAAP) [Software].* Retrieved from `https://github.com/AndreasPrein/MOAAP/tree/V1.0` doi: 10.5281/zenodo.7561616

Rasmussen, R. M., & et al. (in review). The NCAR-USGS 4-km long-term regional hydroclimate reanalysis over the CONUS. *BAMS*.

Reid, K. J., King, A. D., Lane, T. P., & Short, E. (2020). The sensitivity of atmospheric river identification to integrated water vapor transport threshold, resolution, and regridding method. *Journal of Geophysical Research: Atmospheres*, *125*(20), e2020JD032897.

Reid, K. J., Rosier, S. M., Harrington, L. J., King, A. D., & Lane, T. P. (2021). Extreme rainfall in New Zealand and its association with Atmospheric Rivers. *Environmental Research Letters*, *16*(4), 044012.
Rodgers, E. B., Adler, R. F., & Pierce, H. F. (2001). Contribution of tropical cyclones to the North Atlantic climatological rainfall as observed from satellites. *Journal of Applied Meteorology*, *40*(11), 1785–1800.
Rutz, J. J., Steenburgh, W. J., & Ralph, F. M. (2014). Climatological characteristics of atmospheric rivers and their inland penetration over the western United States. *Monthly Weather Review*, *142*(2), 905–921.
Schumacher, R. S., & Johnson, R. H. (2006). Characteristics of US extreme rain events during 1999–2003. *Weather and Forecasting*, *21*(1), 69–85.
Shields, C. A., Rutz, J. J., Leung, L.-Y., Ralph, F. M., Wehner, M., Kawzenuk, B., ... others (2018). Atmospheric river tracking method intercomparison project (ARTMIP): project goals and experimental design. *Geoscientific Model Development*, *11*(6), 2455–2474.
Simmonds, I., & Murray, R. J. (1999). Southern extratropical cyclone behavior in ECMWF analyses during the FROST special observing periods. *Weather and forecasting*, *14*(6), 878–891.
Stern, D. P., & Nolan, D. S. (2012). On the height of the warm core in tropical cyclones. *Journal of the Atmospheric Sciences*, *69*(5), 1657–1680.
Stevens, B., Satoh, M., Auger, L., Biercamp, J., Bretherton, C. S., Chen, X., ... others (2019). DYAMOND: the DYnamics of the Atmospheric general circulation Modeled On Non-hydrostatic Domains. *Progress in Earth and Planetary Science*, *6*(1), 1–17.
Ullrich, P. A., & Zarzycki, C. M. (2017). TempestExtremes: A framework for scale-insensitive pointwise feature tracking on unstructured grids. *Geoscientific Model Development*, *10*(3), 1069–1090.
Ullrich, P. A., Zarzycki, C. M., McClenny, E. E., Pinheiro, M. C., Stansfield, A. M., & Reed, K. A. (2021). TempestExtremes v2. 1: a community framework for feature detection, tracking, and analysis in large datasets. *Geoscientific Model Development*, *14*(8), 5023–5048.
Viale, M., Valenzuela, R., Garreaud, R. D., & Ralph, F. M. (2018). Impacts of atmospheric rivers on precipitation in southern South America. *Journal of Hydrometeorology*, *19*(10), 1671–1687.
Vitart, F., Anderson, J., & Stern, W. (1997). Simulation of interannual variability of tropical storm frequency in an ensemble of GCM integrations. *Journal of Climate*, *10*(4), 745–760.
Waliser, D., & Guan, B. (2017). Extreme winds and precipitation during landfall of atmospheric rivers. *Nature Geoscience*, *10*(3), 179–183.
Wu, X., & Yan, J. (2011). Estimating the outgoing longwave radiation from the FY-3B satellite visible infrared radiometer Channel 5 radiance observations. *Chinese Science Bulletin*, *56*(32), 3480–3485.
Yang, G.-Y., & Slingo, J. (2001). The diurnal cycle in the tropics. *Monthly Weather Review*, *129*(4), 784–801.

Supporting Information for "The Multi-Scale Interactions of Atmospheric Phenomenon in Extreme and Mean Precipitation"

Andreas F. Prein[1], Priscilla A. Mooney[2], James M. Done[1]

[1]National Center for Atmospheric Research

[2]NORCE, Bjerknes Centre for Climate Research

Contents of this file

1. Figures S1 to S4

Introduction

This supplement contains four additional figures containing seasonal frequencies of phenomenon and the relevance of phenomenon for daily precipitation extremes. More detailed information can be found in the figure captions.

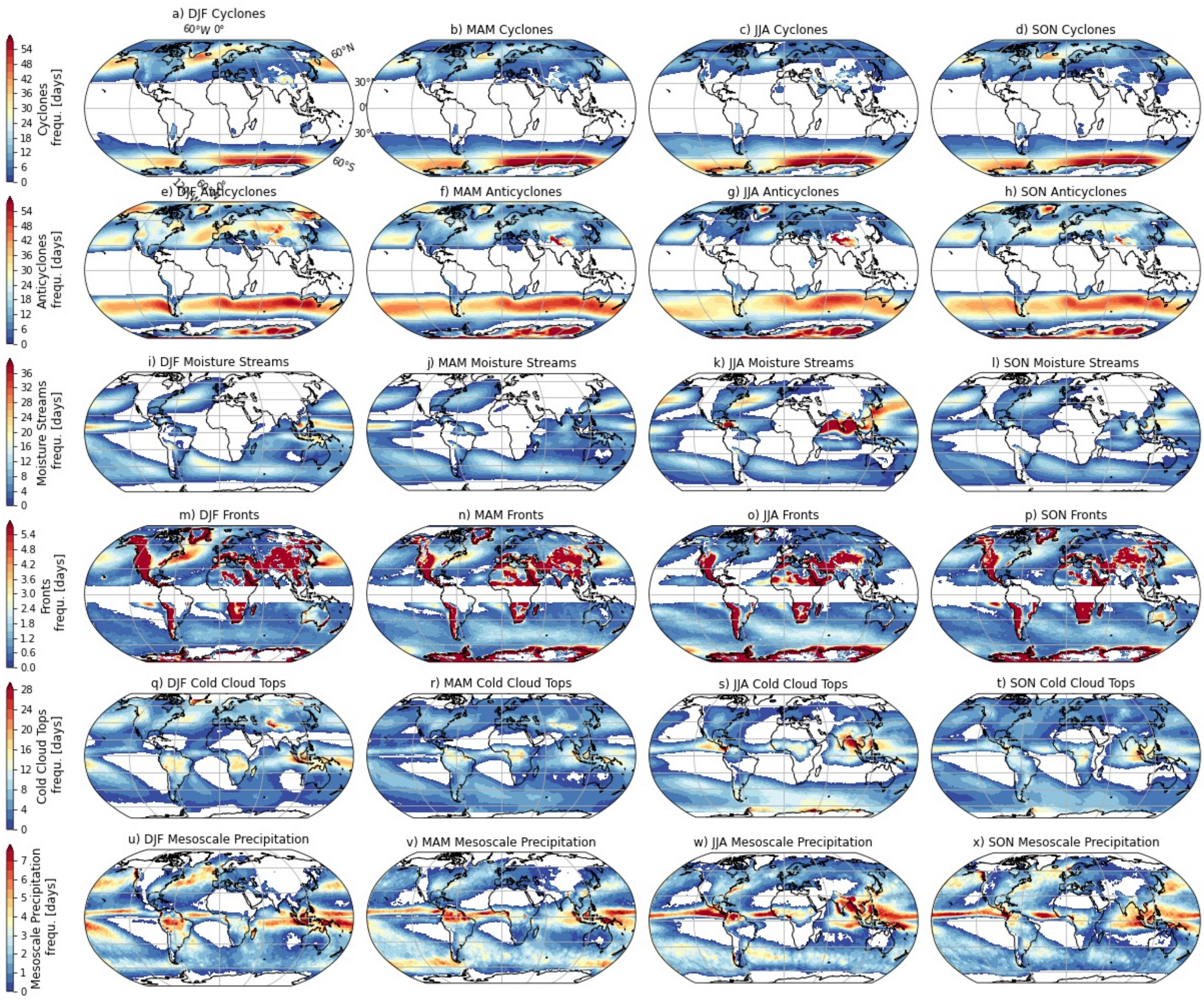

Figure S1. Seasonal frequencies of cyclones, anticyclones, ARs, fronts, MCSs, and TCs features are shown top-down for DJF, MAM, JJA, and SON (top-to-bottom).

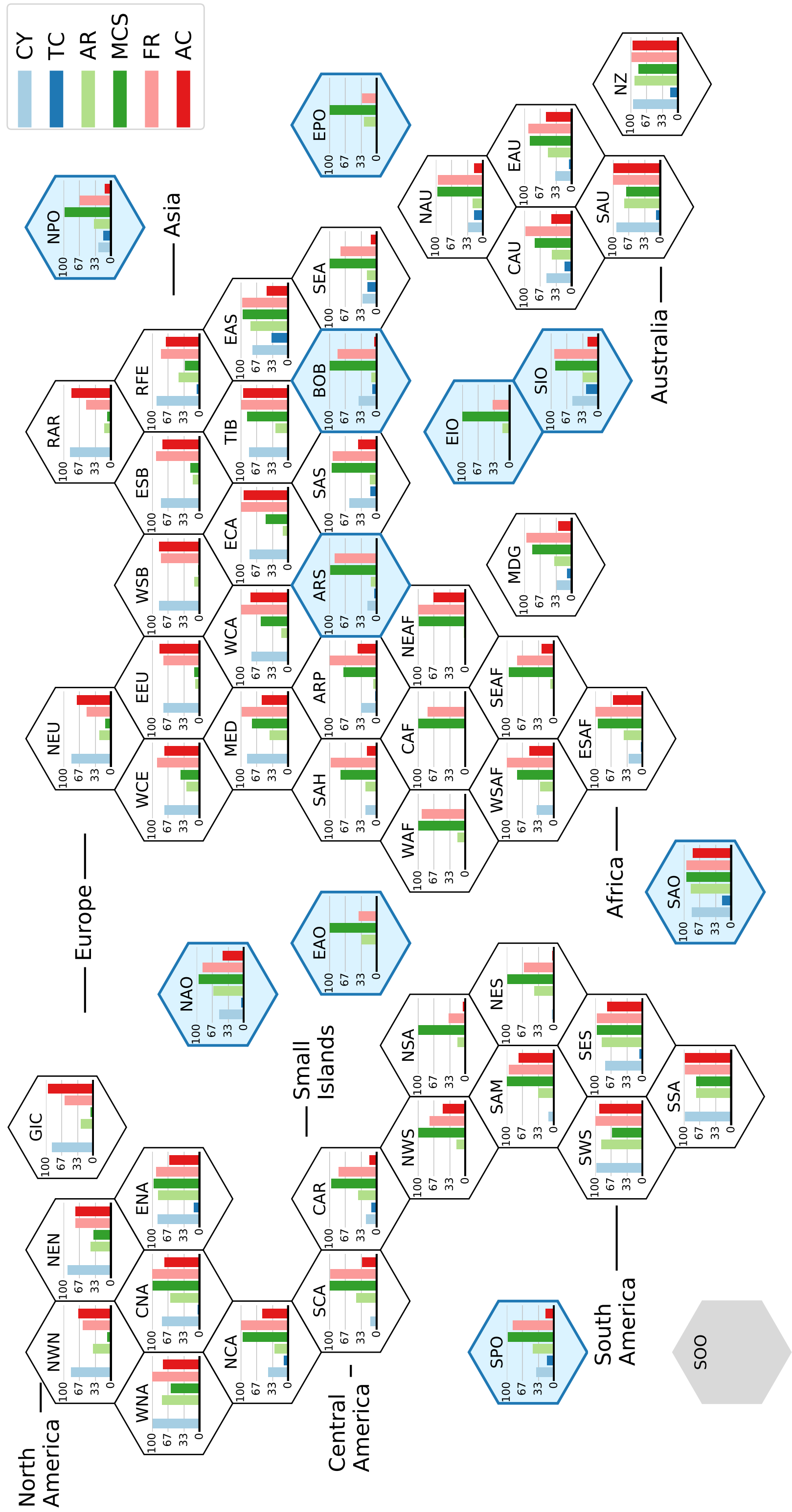

Figure S2. Frequency of features in the vicinity (1,000 km radius) of daily extreme precipitation events in IPCC AR6 regions. We consider the 100 most extreme daily precipitation events in each region based on GPM-IMERG precipitation. Blue hexagons indicate ocean regions and grey hexagons do not contain GPM-IMERG precipitation data. The regions are defined in Iturbide et al. (2020)).

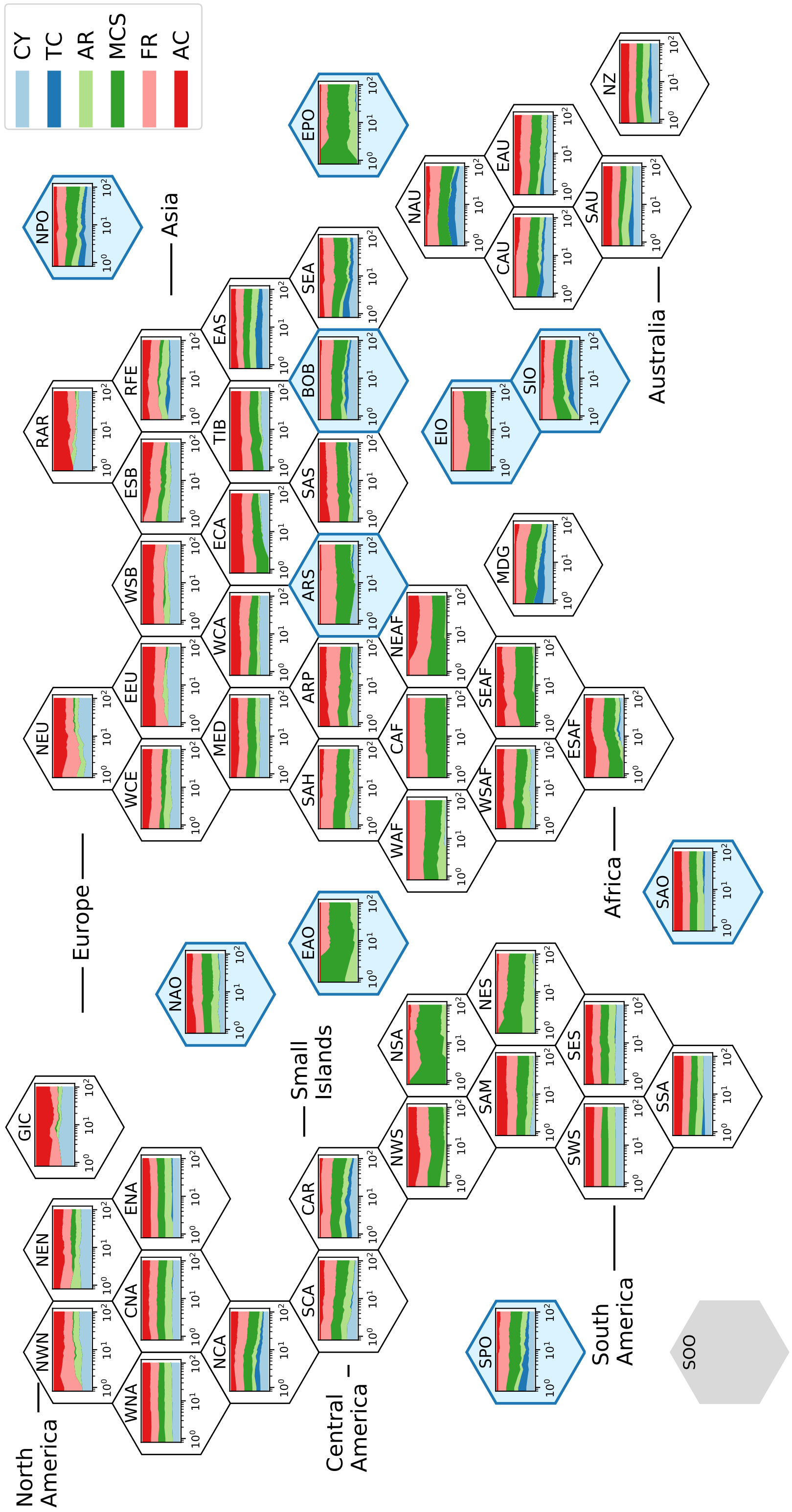

Figure S3. As Fig. S2 but showing the percent contribution (vertical axis) of atmospheric features dependent on the intensity of the extreme precipitation events with the rarest event on the left and all of the 100 most extreme daily precipitation events on the right.

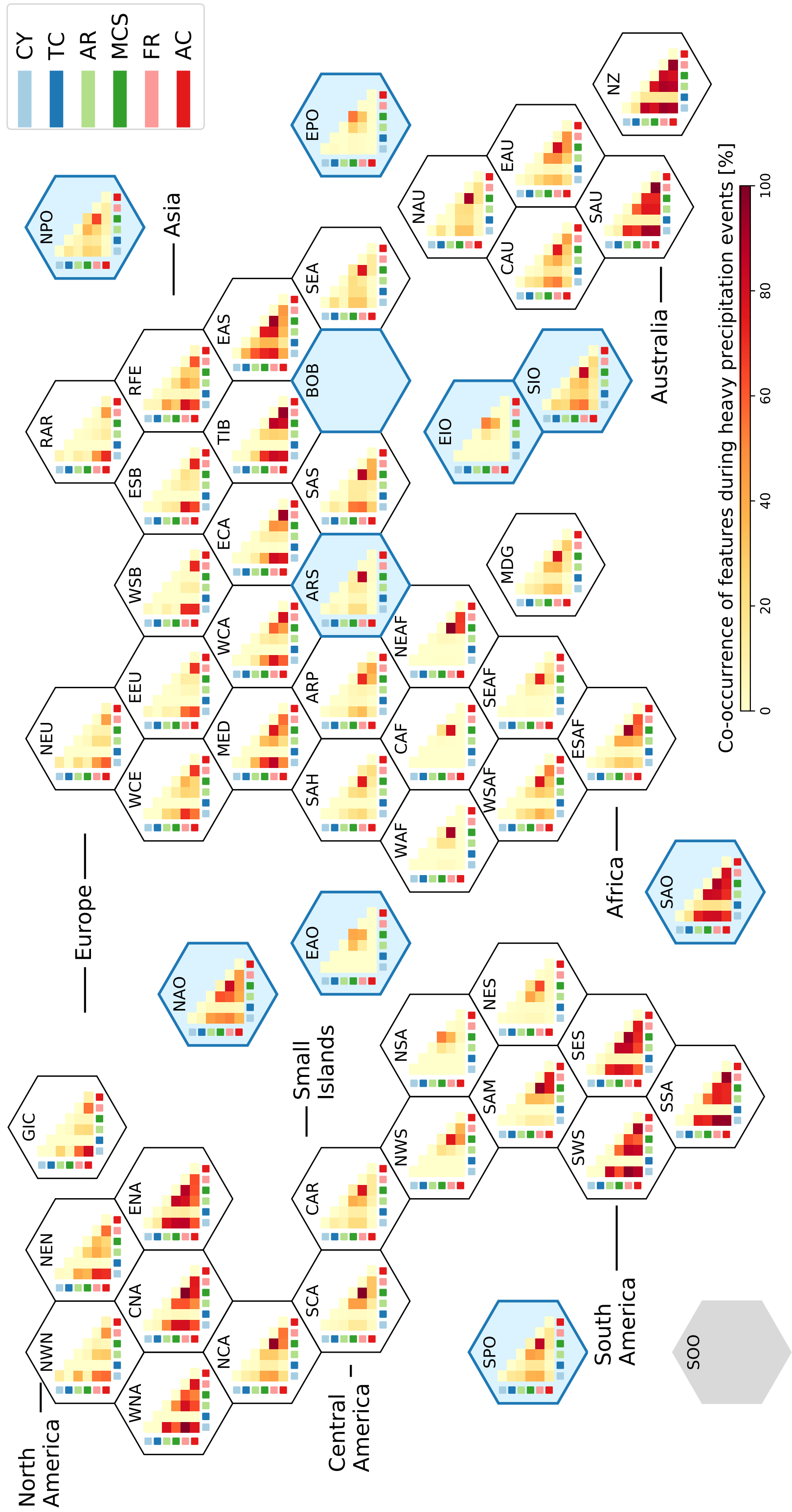

Figure S4. Showing the same data as in Fig. S2 but highlighting the co-occurrence of features during daily extreme precipitation events. The colors in the heatmaps show the percent of the time at which features co-occurred. The colors beneath the x- and y-axis show the feature as indicated in the legend.

References

Iturbide, M., Gutiérrez, J. M., Alves, L. M., Bedia, J., Cerezo-Mota, R., Cimadevilla, E., ... others (2020). An update of IPCC climate reference regions for subcontinental analysis of climate model data: definition and aggregated datasets. *Earth System Science Data*, *12*(4), 2959–2970.

do not specify file extension